

PNNL-37418

# Radiation Stability of MOFs for Noble Gas Capture and Separation

Gamma radiation study on CaSDB and CuBTC MOFs

February 2025

Keerthana Krishnan Matthew J. Hurlock Mark Murphy Sun Hae Ra Shin Kumari Sushmita Praveen K. Thallapally



#### **DISCLAIMER**

This report was prepared as an account of work sponsored by an agency of the United States Government. Neither the United States Government nor any agency thereof, nor Battelle Memorial Institute, nor any of their employees, makes any warranty, express or implied, or assumes any legal liability or responsibility for the accuracy, completeness, or usefulness of any information, apparatus, product, or process disclosed, or represents that its use would not infringe privately owned rights. Reference herein to any specific commercial product, process, or service by trade name, trademark, manufacturer, or otherwise necessarily constitute or imply its endorsement, recommendation, or favoring by the United States Government or any agency thereof, or Battelle Memorial Institute. The views and opinions of authors expressed herein do not necessarily state or reflect those of the United States Government or any agency thereof.

PACIFIC NORTHWEST NATIONAL LABORATORY

operated by

BATTELLE

for the

UNITED STATES DEPARTMENT OF ENERGY

under Contract DE-AC05-76RL01830

Printed in the United States of America

Available to DOE and DOE contractors from the Office of Scientific and Technical Information, P.O. Box 62, Oak Ridge, TN 37831-0062

www.osti.gov ph: (865) 576-8401 fox: (865) 576-5728 email: reports@osti.gov

Available to the public from the National Technical Information Service 5301 Shawnee Rd., Alexandria, VA 22312 ph: (800) 553-NTIS (6847) or (703) 605-6000

email: info@ntis.gov
Online ordering: http://www.ntis.gov

# Radiation Stability of MOFs for Noble Gas Capture and Separation

Gamma radiation study on CaSDB and CuBTC MOFs

February 2025

Keerthana Krishnan Matthew J. Hurlock Mark Murphy Sun Hae Ra Shin Kumari Sushmita Praveen K. Thallapally

Prepared for the U.S. Department of Energy under Contract DE-AC05-76RL01830

Pacific Northwest National Laboratory Richland, Washington 99354

#### **Summary**

The two nanoporous materials, CaSDB and HKUST-1, that show promise as noble gas sorbents were selected as exemplar candidates to radiation stability studies. The CaSDB powders were synthesized in PNNL, and HKUST-1 was obtained from a commercial vendor as Basolite C300. The nanoporous sorbents were fully characterized using X-ray diffraction, gas adsorption analysis, and both FTIR and NMR. The MOFs were then exposed to gamma (y) radiation doses between 100 and 500 Mrad using 60Co at PNNL facilities. Based on our previous calculations, a 600 MW<sub>th</sub> reactor fissioning <sup>233</sup>U is expected to deliver a dose of 64.2 Gy to the sorbent from beta decay of Xe radioisotopes and 132.7 Gy from decay of Kr (50L MOF tank). The current irradiation experiments are an order of magnitude higher than the actual dose. Following irradiation, the same characterizations were performed and compared to the pristine samples to elucidate framework stability trends. XRD patterns showed crystallinity, the long-range order, of both frameworks was maintained. Further Rietveld refinement of the post-exposure XRD patterns demonstrated only small changes in unit cell parameters across all doses. However, BET surface area measurements of the irradiated MOFs showed substantial decreases compared to the pristine materials. This contrast with the XRD, SEM results illustrated by the gas adsorption analysis indicated some structural changes had occurred to the local structure, resulting in primarily porosity changes. FTIR spectra of the irradiated MOFs were used to examine the local structures within the frameworks. FTIR analysis showed little to no change in the coordination and bonding of the MOFs, aligning with XRD patterns. Altogether, these results demonstrated that the framework structure of both MOFs was stable up to 500 Mrad as little to no change was observed in both the long-term and local structures. However, the porosity of the MOFs was acutely sensitive to the radiation, which indicates that the subtle structures changes that have a skewed impact on the pores are occurring within MOFs. Though a mechanism could not yet be developed with the available data, it likely involves radiation-induced local-structural changes that cause blocking of the internal porosity without substantial changes to the framework. Further work is needed to reproduce the results and impact of radiation on noble gas adsorption.

The project goals moving forward are to i) irradiate engineered forms of the CaSDB and HKUST-1 MOFs to elucidate effects of material processing on radiation stability, ii) expand the characterization methods post-irradiation to also include (XPS) and EXAFS to better determine local changes within the MOF structure, and iii) quantify internal surface areas post irradiation using apparent BET surface areas by changing analysis gas from  $N_2$  to  $CO_2$  and increasing analysis temperature from 77 K to 273 K.

Summary

#### **Acronyms and Abbreviations**

MOF metal-organic framework

Xe Xenon Kr Krypton

PNNL Pacific Northwest National Laboratory

BTC benzenetricarboxylic acid SDB 4,4'-sulfonyldibenzoic acid

CaSDB calcium-4,4'-sulfonyldibenzoate

CuBTC copper–1,3,5-benzenetricarboxylate (as so known as HKUST-1)

PXRD powder X-ray diffraction

SEM scanning electron microscopy
BET Brunauer–Emmett–Teller

NMR nuclear magnetic resonance spectroscopy
FTIR Fourier transform infrared spectroscopy

mmol millimoles g gram

NU-1000 zirconium-4,4',4"-(Pyrene-1,3,6,8-tetrayl)tetrabenzoic acid

(Northewestern University 1000)

UiO-66 zirconium-benzenedicarboxylic acid

OMMT organo-montmorillonite

BASF Badische Anilin und Soda Fabrik

eV electron volt

MeV mega electron volt
Z atomic number
CNT carbon nanotube
FWHM full width at half max

XPS X-ray photoelectron spectroscopy

BDC benzene dicarboxylic acid

H₄TBAPy 4,4',4"'-(Pyrene-1,3,6,8-tetrayl)tetrabenzoic acid

## **Contents**

| Sumi | ımary                              | i   |
|------|------------------------------------|-----|
| Acro | onyms and Abbreviations            | iii |
| 1.0  | Introduction                       |     |
| 2.0  | Preparation of Noble Gas Sorbents  | 3   |
| 3.0  | Sorbent Radiation Experiments      |     |
| 4.0  | Impacts of γ-Radiation on Sorbents |     |
|      | 4.1 CuBTC                          | 10  |
|      | 4.2 CaSBD                          | 17  |
| 5.0  | Conclusion                         | 21  |
| 6.0  | Future Work                        | 21  |
| 7.0  | References                         |     |
| 8.0  | Acknowledgements                   | 24  |

## **Figures**

| Figure 1: Comparison of PXRD patterns of (A) CaSDB and (B) CuBTC with the respective simulated patterns. * Reflection represents unreacted starting ligand  | 3  |
|---|----|
| Figure 2: SEM image of pristine powders of (A) CaSDB and (B) CuBTC.   | 4  |
| Figure 3: Nitrogen gas adsorption isotherms and calculated BET surface areas of pristine CuBTC (blue) and CaSDB (orange) at 77K. The closed and open data points represent adsorption and desorption, respectively  | 5  |
| Figure 4: Gas adsorption isotherms of Xe (orange) and Kr (blue) for pristine powders of (A) CaSDB and (B) CuBTC, at room temperature (298 K).   | 5  |
| Figure 5: Optical images of pristine powders of (A) CaSDB and (B) CuBTC   | 6  |
| Figure 6: Diagram of (A) the glass vial used in the radiation experiments and images of pristine MOF loaded vails containing (B) CuBTC and (C) CaSDB  | 6  |
| Figure 7: Radiation exposure chamber at PNNL.   | 8  |
| Figure 8: (A) Photograph of the wire mesh testing apparatus within the radiation chamber, (B) illustration of the ten dose locations, (C) the MOF samples loaded into the test chamber with corresponding IDs.  | 8  |
| Figure 9: Images of radiation exposed vials (doses from left to right 100, 200, 300, 400, and 500 Mrad:) for (A) CaSDB and (B) CuBTC powders  | 9  |
| Figure 10: Images of pristine (Left) and 500 Mrad (right) radiation exposed CuBTC samples.  | 10 |
| Figure 11: Light microscope images of CuBTC post-irradiation at 100, 200, 300, 400, and 500 Mrad  | 10 |
| Figure 12: Comparison of SEM image of (A) pristine CuBTC to irradiated CuBTC powders at (B) 100, (C) 200, (D) 300, (E) 400, and (F) 500 Mrad  | 11 |
| Figure 13: Comparison of (A) PXRD patterns of CuBTC powders pre- and post-radiation with (200) and (220) reflections highlighted green and blue, respectively, and (B) relative reflection ratio of $R_{(200)}/R_{(220)}$ of irradiated samples compared to pristine CuBTC; (C) illustration of the (200) plane (blue) and (220) plane (green) of CuBTC | 12 |
| Figure 14: FTIR spectra of pre- and post-irradiation CuBTC samples between (A) 400 and 1800 cm <sup>-1</sup> with the green highlighted region representing the free BTC carboxylic acid shift and (B) a zoomed spectra depicting the changes to the free BTC carboxylic acid shift   | 13 |
| Figure 15: Comparison of (A) N <sub>2</sub> gas adsorption isotherms at 77K of pre- and post-<br>irradiation CuBTC samples and (B) the relative BET of CuBTC post-<br>radiation   | 14 |
| Figure 16: Comparison of pore volume distribution of CuBTC pre- and post-irradiation.  All data is offset by 2 cm <sup>3</sup> /g   | 15 |
| Figure 17: Gas adsorption isotherms of irradiated CuBTC powders at -78°C for the noble gases (A) Xe and (B) Kr  | 16 |
| Figure 18: Photographs of pristine CaSDB (left) and CaSDB post 500 Mrad irradiation dose. (right)   | 17 |

Figures

| Figure 19: Optical images radiation exposed CaSDB samples  | 17 |
|--|----|
| Figure 20: SEM images of CaSDB powders pre- and post-irradiation   | 18 |
| Figure 21: FTIR spectra of pristine and irradiated CaSDB samples. The green highlighted peak at 1680 cm <sup>-1</sup> represents the free linker carboxylic acid chemical shift.   | 18 |
| Figure 22: Comparison of PXRD patterns of CaSDB powders pre- and post-radiation  |    |
| Figure 23: Percentage change in unit cell parameters a (red circles), b (yellow triangles), and c (blue squares) from Rietveld refinement of CaSDB post-irradiation.  The grey dashed line represents the pristine cell parameters | 20 |
| Figure 24: N <sub>2</sub> gas adsorption isotherms of pristine CaSDB and selected CaSDB post-irradiation at 200, 300, and 400 Mrad   | 21 |
|  |    |
| Tables   |    |
| Tables      Table 1: Explanation of radiation dosages and corresponding units.   | 7  |
|  |    |
| Table 1: Explanation of radiation dosages and corresponding units  | 8  |
| Table 1: Explanation of radiation dosages and corresponding units  | 9  |
| Table 1: Explanation of radiation dosages and corresponding units  | 9  |
| Table 1: Explanation of radiation dosages and corresponding units  | 12 |

Tables

#### 1.0 Introduction

When an incident gamma ( $\gamma$ ) ray encounters a material, several interactions occur. Elastic scattering or Rayleigh scattering is a phenomenon where the photon is scattered without any loss in energy. There is no considerable absorption leading to no permanent energy uptake by the material. In the case of inelastic scattering or Compton scattering, the incident photon imparts energy to the outermost electron and the photon is now scattered with a reduced energy translating to a longer wavelength. The ejected electron recoils with the energy lost by the photon. The third possible phenomenon is photoelectric effect where the incident photon ejects a core electron from an atom. The photon energy is used to overcome the electrons binding energy. The excess energy thus becomes the kinetic energy of the ejected photoelectron. The ionized atom may return to ground state by emitting characteristic radiation or via the Auger effect. This effect is observed to be most dominant for high Z (effective atomic number) materials at low energies (typically <500 keV). Pair production is another phenomenon where the photon with energy  $\geq$  1.02 MeV interacts with a nucleus or electron to produce an electron-positron pair. The electron is absorbed by a positive ion, the positron interacts with another electron thus generating two annihilation photons of 511 keV each.

A good radiation shield is one that can attenuate, absorb, or block the maximum part of incident radiation. All these effects are described by the proper cross-section values of the materials which is a measure of the probability that a scattering will occur. Light element-based materials, like carbon, have much smaller values of cross sections because their nucleus contains much fewer protons and much fewer electrons around them, making them much less useful as a shield against ionized radiation. A material with higher density and Z increases its probability of interaction with incident photon at the same time creating secondary particles whereas materials with lower Z and lower density can still be used if they are used in sufficient thickness. So, a well-thought decision would be to develop a novel composite combination material including bismuth oxide nanoparticles, carbon nanotubes, graphene oxide flakes.<sup>1</sup>

Polymers which are lightweight and durable, offer many appealing physical and mechanical properties in turn radiation resistant properties. The main phenomenon by which degradation occurs in polymers in radiation-induced free radical formation. When the photon interacts with the particle, a free radical process is initiated by the polymer backbone due to the absorbed ionization energy. The properties of the material are thus altered because of chain scission and cross linking observed in materials like OMMT nanocomposites. As a result of gamma radiation, the properties of the polymer degrade, then slightly improve and rapidly degrade again because of competition between chain scission and cross linking.<sup>2</sup> Addition of filler material in polymers<sup>3</sup> is an alternative to better their performance depending on certain properties such as uniform dispersion of the filler material within the polymer matrix, the type of interaction between the parent material and the filler and size effects from the filler as smaller sized fillers avoid creating large stress concentrations. CNT has been reported as a filler material because of its higher tensile strength and elastic modulus in addition to being thermally and electrically conductive. Some other antirad compounds such as 2-Vinylnaphthalene,3 4-vinylbiphenyl, aromatic diacetylenes, and oxygen have been used to reduce the effects due to gamma radiation by making scavenging radicals and intermediates to prevent polymer cross linking.<sup>2</sup>

In the case of MOFs, there are certain properties and functional groups to look closely to understand its radiation stability. An initial indication of degradation in MOFs is broadening in its X-ray diffraction pattern because of increase in FWHM values because of loss of crystallinity. Though PXRD would be an initial assessment of the radiation stability in MOFs, local coordination

is not affected particularly in lower radiation dosages and common techniques such as PXRD, IR or Raman become less useful. Thus, advanced characterization techniques such as XPS could be used to observe binding energy shifts as these are indicative of disintegration of metal clusters. Tracking the metal clusters are crucial because, even if one of the three metal clusters are intact, the material could be stable to radiation and indicate crystallinity from PXRD. Any decrease in electron density is also indicative of partial breakage of C–C, C–H, C–O and C=O bonds.

MOFs that have organic struts with extended π-systems which promote high energy delocalization bind strongly to Lewis acid sites and increase its stability. A higher linker connectivity and low node density in a MOF leads to better stability when exposed to radiation. It has been observed from studies that metals that have lower photon cross section have a lower stability as they tend to have a lower surface area. For example, aluminum which has a photon absorption cross section (indicative of probability of interaction) of 14.20 cm<sup>2</sup>/g is better than copper with an absorption cross section of 3.55 cm<sup>2</sup>/g. MOFs that have aromatic linkers promote delocalization and energy dissipation leading to better stability. Similarly, the presence of electron donating group in MOFs show higher radiation stability. Presence of defects in a crystal although an indication of imperfection, could also help with dissipation of energy which would help with increasing the radiation stability of the material. As closer metallic atoms attenuate the generated electrons better, it can also be inferred that the metal nodes concentration per unit volume needs to be higher for more stable materials. Delocalization is a process in π-systems where adjacent bonds are overlapped by p-orbitals thus increasing its stability as the electrons now get spread out over a larger space than being confined. The stabilization of the  $\pi$ -systems may come from the OH groups present in the MOF itself. Similarly, studies have shown that unmodified organic linkers or ligands have higher stability than single groups.

The mechanism by which a MOF encounters radiation is generally that the radiation is first absorbed by the metal node and then transferred to the linkers. This indicates that as the node density decreases, the absorption of radiation also decreases. For example, in a study with UiO-66 and NU-1000,<sup>4</sup> it was observed that UiO-66 with a 12-connected node, which linker has one benzene ring is less stable than NU-1000 with an 8-connected node that linker has four benzene rings. The length of their corresponding linkers i.e., BDC and H<sub>4</sub>TBAPy are 5.77 Å and 12.08 Å respectively. It was observed from the study that the longer the linker was, the lower the node density thus the more radiation stable the framework. Higher node connectivity causes less degradation thus exhibits good stability. On the other hand, low node connectivity causes radiation in nodes to spread to dangling bonds such as OH and H<sub>2</sub>O rather than spreading damage to the linkers.

The stability of MOFs used as nanoporous sorbents is crucial for practical applications. Radiation stability is required for MOFs used in the processing and separation of nuclear reactor off-gas processes. Only a handful of MOFs have been tested under high radiation doses and no examination of how these effects noble gas separation has been performed. Here in, the two exemplar noble gas sorbents CaSDB and CuBTC are exposed with high doses of gamma radiation and their structures and properties are characterized post irradiation. Based on our previous calculations, a 600 MW<sub>th</sub> reactor fissioning <sup>233</sup>U is expected to deliver a dose of 64.2 Gy to the sorbent from beta decay of Xe radioisotopes and 132.7 Gy from decay of Kr (50L MOF tank). The current irradiation experiments on these two MOFs are an order of magnitude higher than what we expect in the real applications.

#### 2.0 Preparation of Noble Gas Sorbents

Through characterization of the pristine sorbents was first performed to obtain a baseline for the materials properties. The nanoporous MOF sorbents were either purchased, in the case of CuBTC (commercially sold by BASF as Basolite C300), or synthesized following literature, in the case of CaSDB.<sup>5</sup> Prior to radiation exposure, the as-made and as-purchased samples were examined for purity using PXRD. As shown in

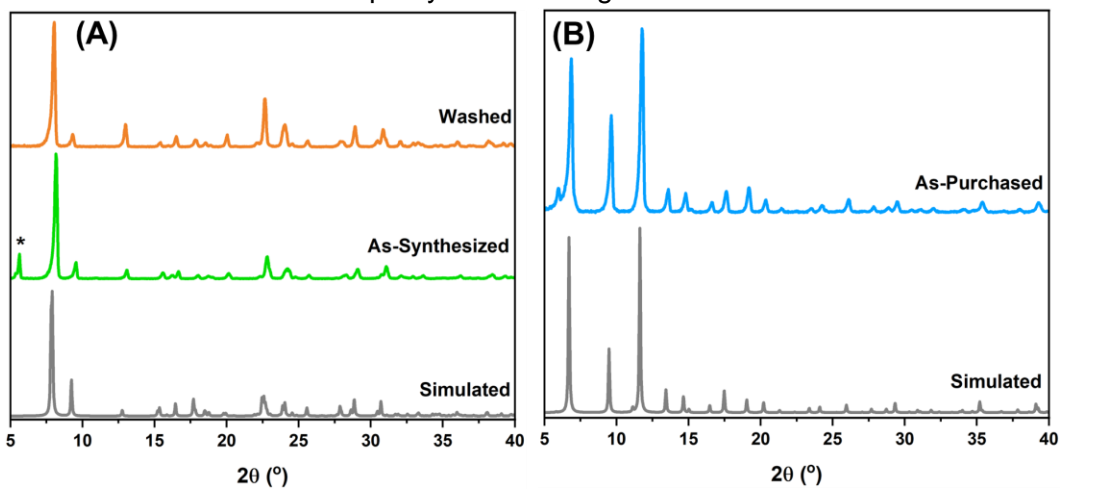


Figure 1A, the synthesized CaSDB powders were found to contain unreacted linker, as indicated by an additional peak around 5.5° 20 in the PXRD pattern. This is likely a result of the low solubility of the SDB linker in the ethanol at ambient temperatures. To remove the unreacted linker, additional washing of synthesized CaSDB powder was performed. First the MOF was suspended in DMF for 1 hour while stirring. Then, the suspension was centrifuged and the DMF was removed. Next, the DMF-washed powder was washed with three times with methanol followed by stirring in fresh methanol for 24 hours at room temperature. The methanol was removed with by centrifuge and the powder was dried under reduced pressure and heating. After the additional cleaning with DMF, the SDB reflection in the CaSDB XRD patterned disappeared as shown in

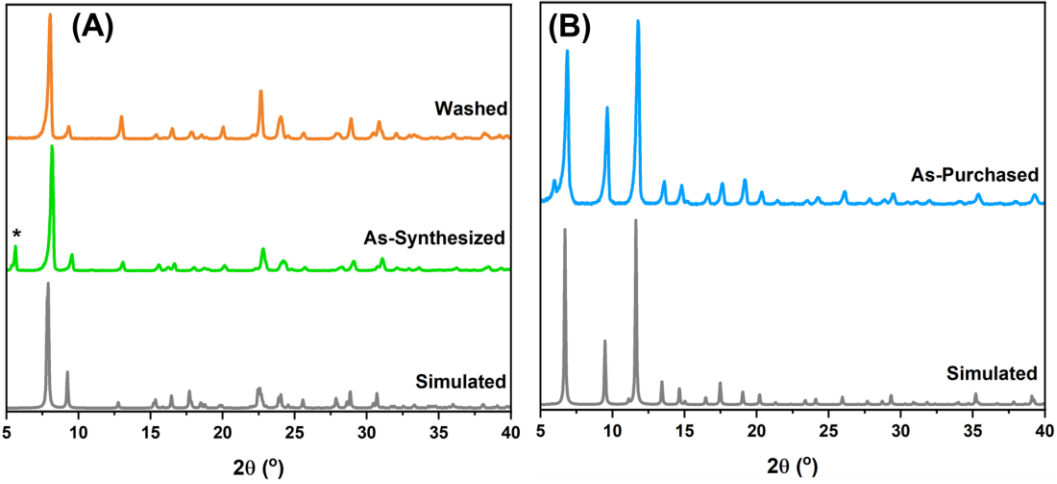
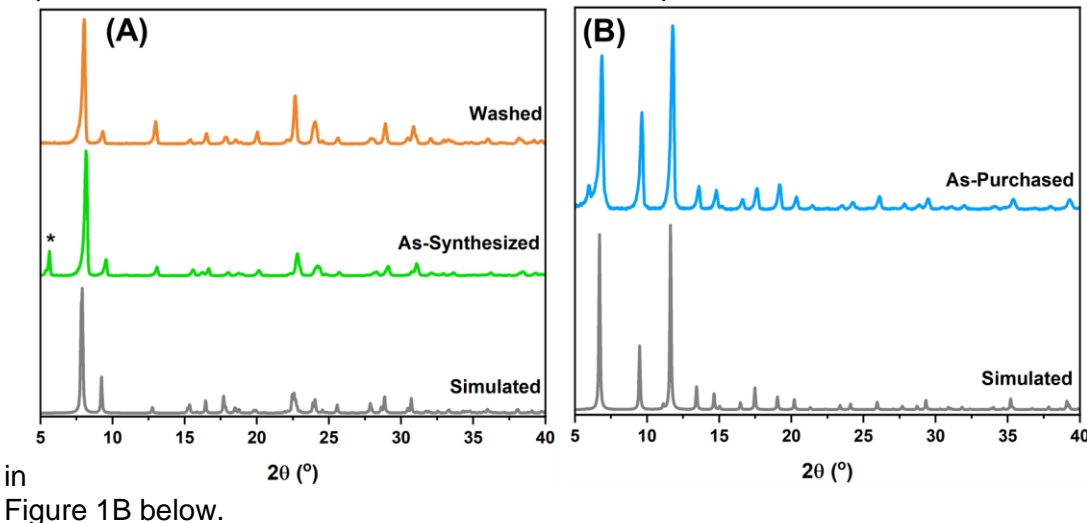


Figure 1A (orange colored PXRD pattern). The XRD pattern now matched with the simulated pattern from the literature and indicated pure phase CaSDB. All further characterization was performed on the washed CaSDB. The received CuBTC powders did not exhibit any apparent



impurities from PXRD, and the obtained diffraction pattern matched with the literature, <sup>6</sup> as shown

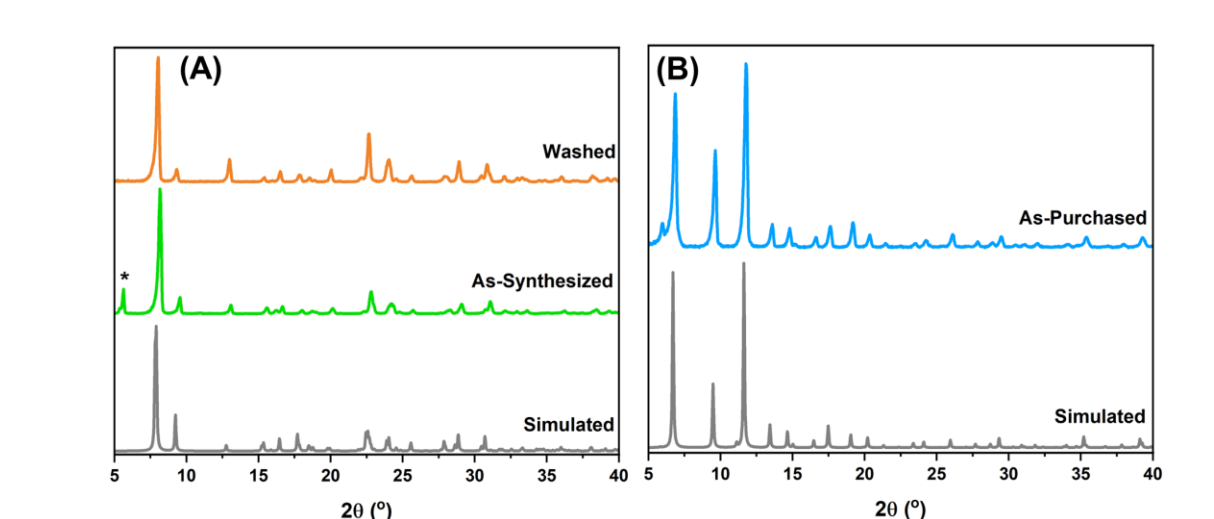


Figure 1: Comparison of PXRD patterns of (A) CaSDB and (B) CuBTC with the respective simulated patterns. \* Reflection represents unreacted starting ligand.

**2**θ (°)

Morphological examination of the pristine MOF powders was also performed using electron microscopy to visualize surface changes and identify signs of degradation.<sup>7</sup> As a baseline, SEM images of the pristine sorbents were obtained using a JEOL JSM-7001F field emission SEM

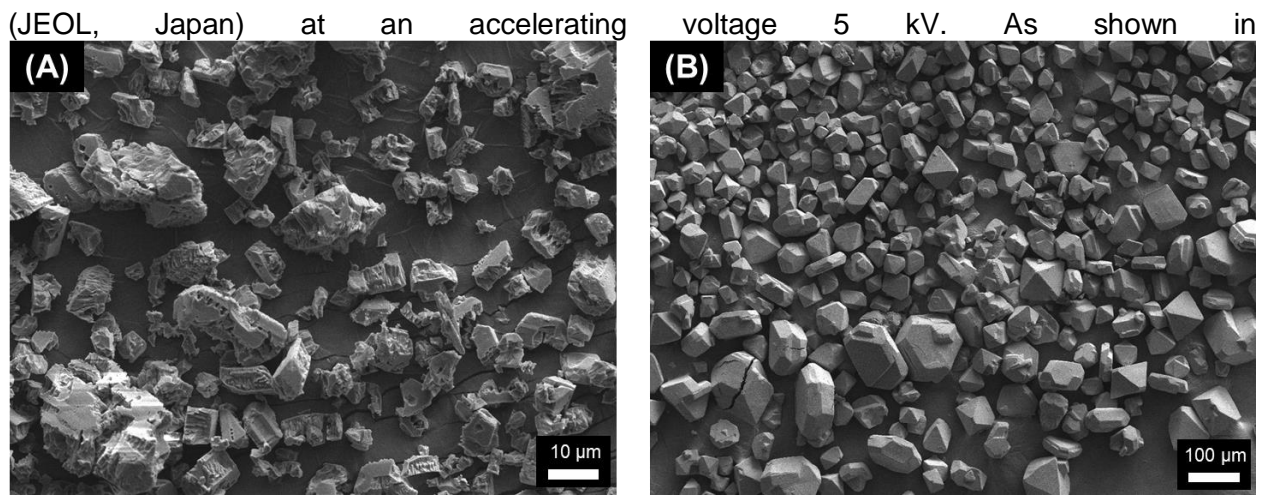


Figure 2A, the pristine CaSDB powder was comprised of particles of irregular shapes and varying sizes (ranging from approximately 2 to 30 μm). This irregularity in particle morphology and size was consistent with previous reports and is likely a result of the harsh synthetic conditions of CaSDB. (180°C) for 3 days) 5 μm contract. CuRTC as shown in

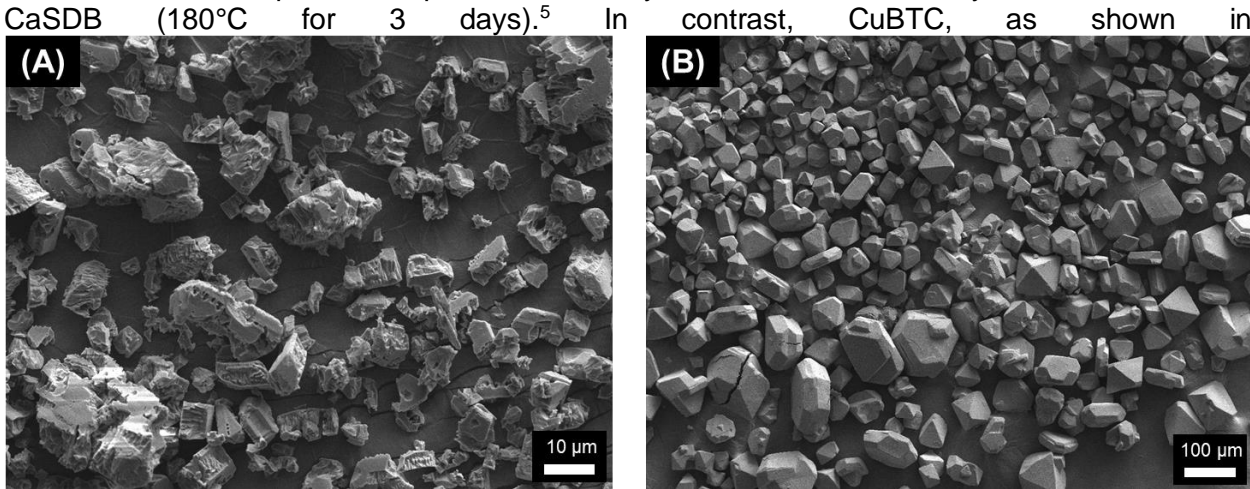


Figure 2B, was comprised of primarily octahedral crystallites, typical of the MOF, that were tens of microns in size. Similarly, the purchased CuBTC showed a wide range of crystallite sizes, a common result of industrial synthesis of MOFs.

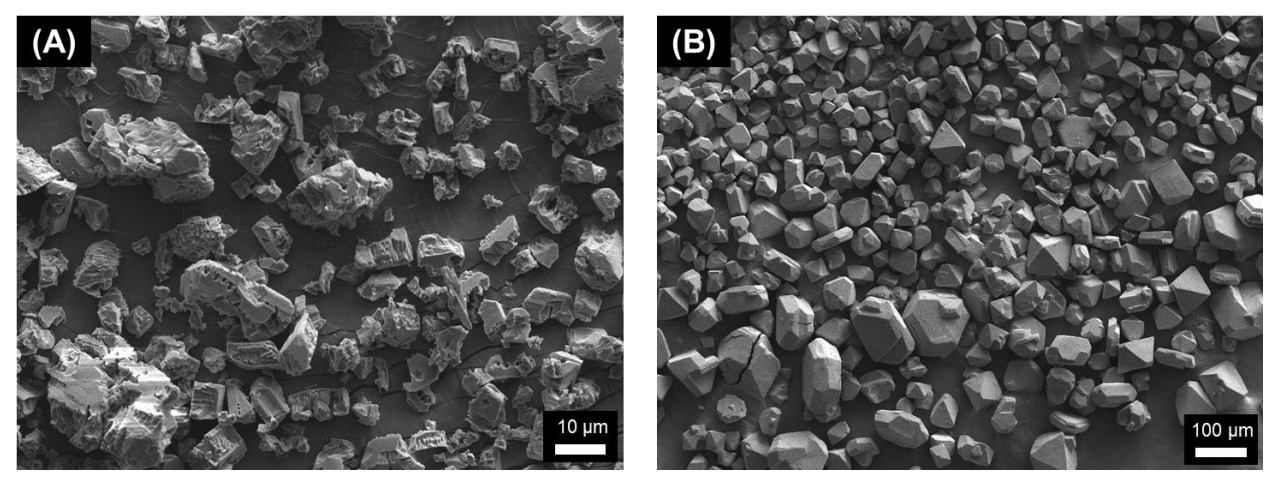
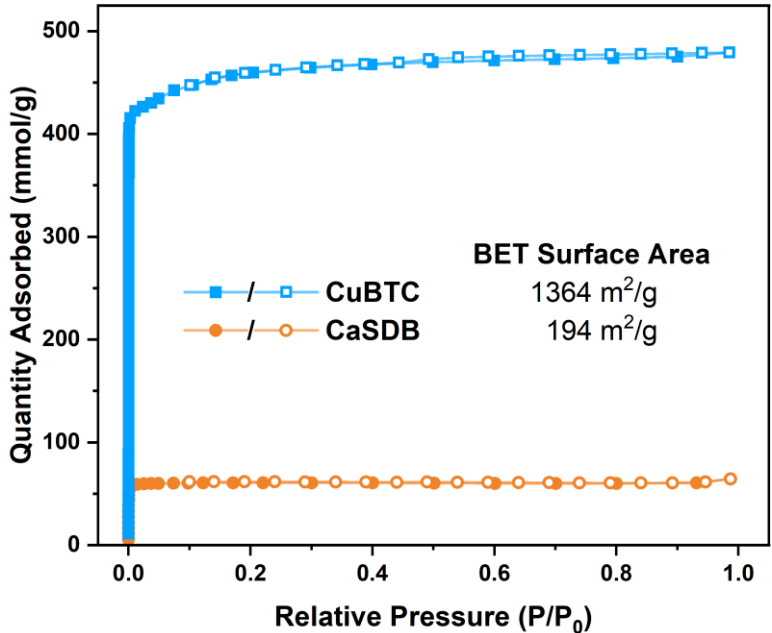


Figure 2: SEM image of pristine powders of (A) CaSDB and (B) CuBTC.

A key objective of this work was to elucidate changes in the porosity of the sorbents when exposed to radiation. Therefore, the textural properties of the pristine sorbents were examined. First, N<sub>2</sub> gas adsorption isotherms were obtained at 77 K and BET surface areas were calculated



from the isotherm data. As shown in

Figure 3, the CaSDB and CuBTC exhibit the expected type 1 isotherms indicative of a microporous structure. The calculated BET surface areas were 194 m²/g and 1364 m²/g pristine CaSDB and CuBTC, respectively. These values align well with previous reports, 5,8 and were used as a baseline for examination of porosity changes post-irradiation. Additionally, the adsorption isotherms of the noble gases Xe and Kr were collected for the pristine sorbents. Figure 4 shows the room temperature (298 K) adsorption isotherms of Xe and Kr for the pristine CaSDB and CuBTC powders. Both materials showed larger Xe uptakes compared to Kr that aligned well with previous reports. For CaSDB, the Xe uptake at X mbar was 1.4 mmol/g compared to 1 mmol/g for Kr at the same pressure. CuBTC showed a larger Xe uptake of  $\approx$  4 mmol/g compared to CaSDB but a similar Kr uptake of 1 mmol/g at 1 bar. This resulted in Xe/Kr adsorption ratios at 1 bar of 1.6 and 4.3 for CaSDB and CuBTC, respectively. These results were used as baseline properties of the two MOFs and all changes observed post-irradiation were relative to these values.

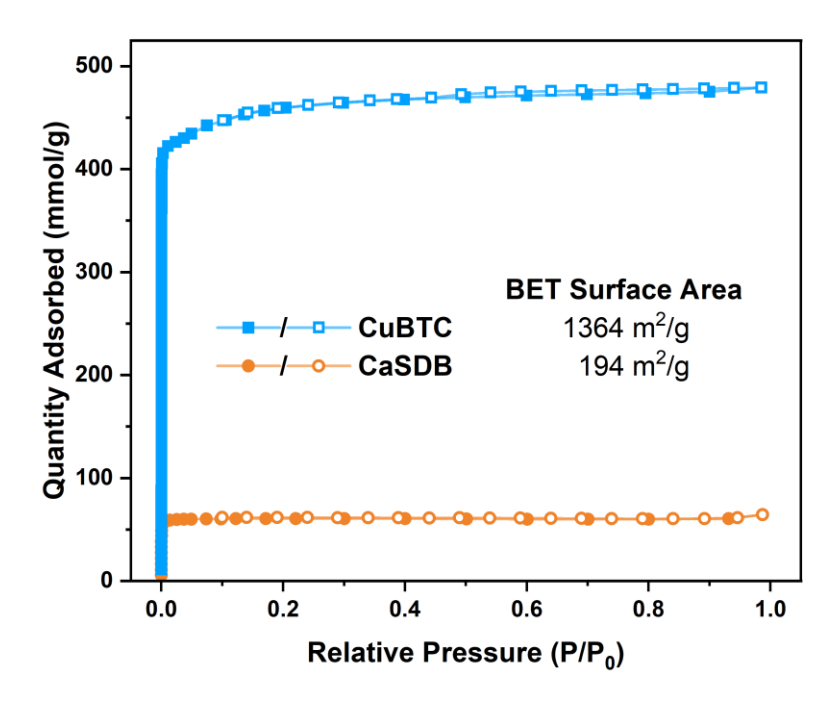


Figure 3: Nitrogen gas adsorption isotherms and calculated BET surface areas of pristine CuBTC (blue) and CaSDB (orange) at 77K. The closed and open data points represent adsorption and desorption, respectively.

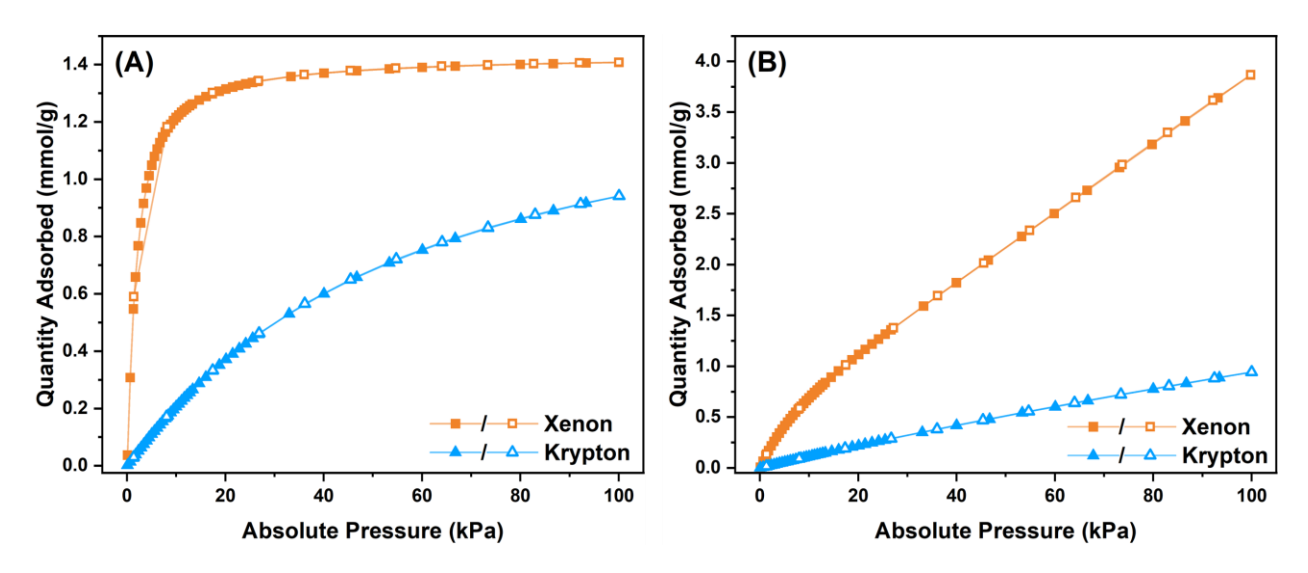


Figure 4: Gas adsorption isotherms of Xe (orange) and Kr (blue) for pristine powders of (A) CaSDB and (B) CuBTC, at room temperature (298 K).

Color changes are a common sign of material degradation. Therefore, optical images and photographs of the pristine samples were collected. As shown in Figure 5 a light microscope at a magnification of 500x. This specific magnification was chosen since higher magnification resulted in unclear or reflective images. The quality and color of optical images also depends on the angle of light used because of issues caused due to shadowing. Pristine CaSDB is an off-white color while pristine CuBTC is a teal-blue color.

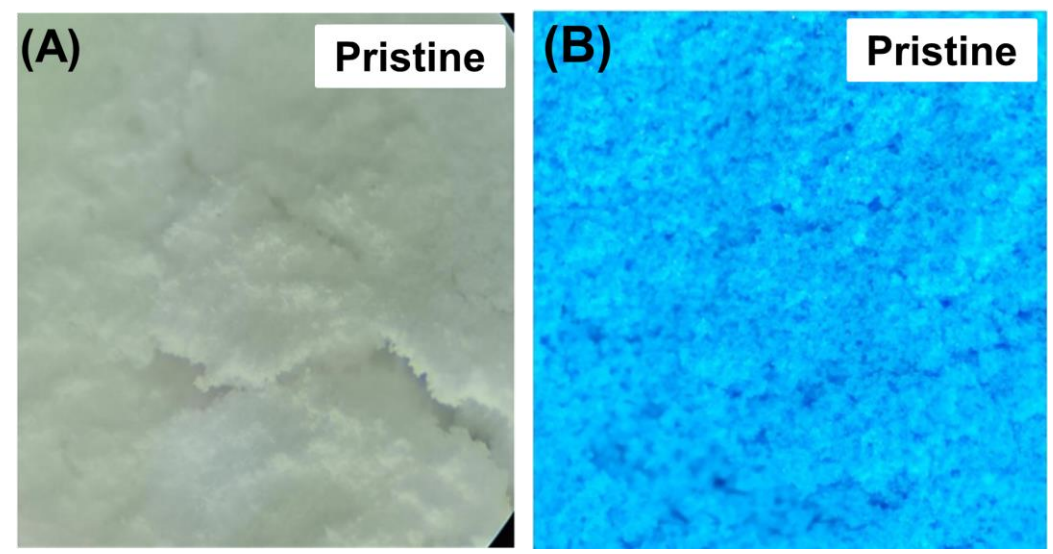


Figure 5: Optical images of pristine powders of (A) CaSDB and (B) CuBTC.

#### 3.0 Sorbent Radiation Experiments

Irradiation of the MOF sorbents was performed at PNNL facilities using a <sup>60</sup>Co source. Once the pristine MOFs were fully characterized and baseline properties were determined irradiation experiments were performed on the bulk powders. Optimization of the experimental geometry was required 0.25 dram glass vials, shown in Figure 6a. Using these vails, 250 mg of the MOF powders were loaded for each dose without degassing see Figure 6B – C.

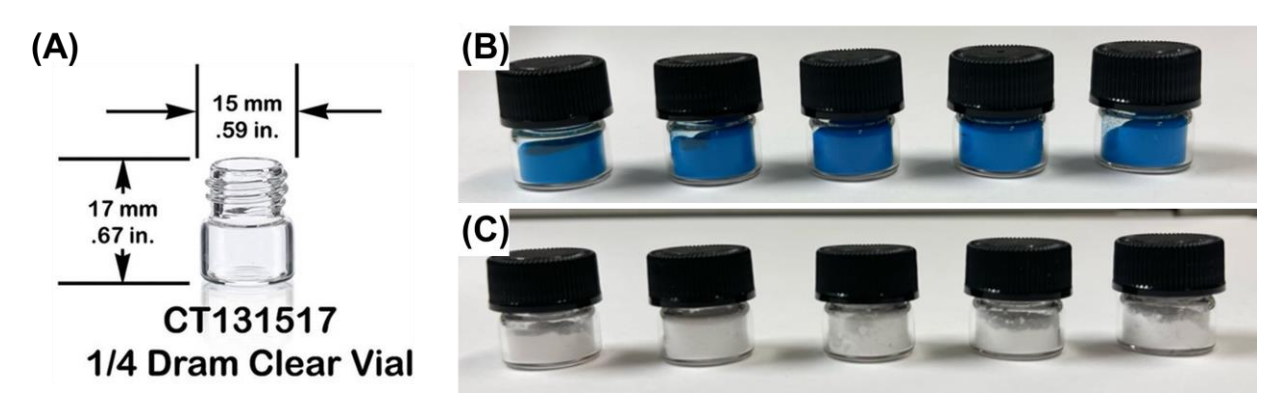


Figure 6: Diagram of (A) the glass vial used in the radiation experiments and images of pristine MOF loaded vails containing (B) CuBTC and (C) CaSDB.

Table 1 indicates the explanation of each of the terminologies used for understanding the radiation exposure. Five doses (100, 200, 300, 400, 500 Mrad) were selected to elucidate structure-property changes as a function of dose amount. Table 1 provides a summary of the radiation dose units and what each represents. These doses were selected to allow for comparison to other reported studies of irradiation stability of MOFs.<sup>4, 9-11</sup> Samples were removed from the experiment over the course of the exposure as the desired doses were reach.

Table 1: Explanation of radiation dosages and corresponding units.

| "Dose" Type  | Formula and<br>Explanation   | SI Units  | Non-SI Units   |
|--|--|---|--|
| Exposure, <b>X</b><br>(Charge per<br>unit volume)              | $X = \Delta Q/\Delta m$ , Where $\Delta Q$ is the electric charges (positive and negative ions) made by the incident radiation in a specified volume of air, and $\Delta m$ is the mass of air. The relationship between <i>Absorbed Does</i> and <i>Exposure Dose</i> is $D = f \cdot X$ , where $D = f \cdot X$ is absorbed dose and $f = f \cdot X$ is a coefficient of a value dependent on type of medium $(f < 1)$ | Couloumb/<br>kilogram,<br><b>C/kg</b>               | Roentgen, R<br>(1 R = 2.58x10 <sup>-4</sup><br>C/kg) |
| Air KERMA, <b>K</b><br>(energy per<br>mass of air)             | Kinetic Energy released In a Medium. The sum of the initial kinetic energy of all charged ionizing particles liberated by uncharged ionizing radiation in a give mass of air. In the region of CPE, KERMA and Absorbed dose are equal.   |   | rad<br>(100 rad = 1 Gy)                              |
| Absorbed Dose, <b>D</b><br>(energy per<br>unit mass of medium) | $D = \Delta E/\Delta m$ , Where $\Delta E$ is the energy lost form the radiation beam, $\Delta m$ and is the mass of the medium into which the energy is absorbed.   | Joule/kg,<br><b>J/kg</b><br>(1 J/kg =<br>Gray (Gy)) | rad<br>(100 rad = 1 Gy)                              |

Figure 7 shows an image of the radiation exposure chamber where, at the pore opening, the samples were placed for irradiation. To hold the sample vials in place a wire mesh was cut into a circle and shaped into a concave geometry of  $\sim$ 5.2 cm radius, then taped within the HEF collimator, see Figure 8A. A micro-volume ionization chamber (Exradin Model A16) was then used to measure/map the dose rate at various locations across the wire grid for Co-60 source 318-548 ( $\sim$ 8000 curies). Due to the asymmetric geometry/construction of the source capsule and transport pipe and collimator plug, the dose rates across the wire grid were not uniform (i.e., not within measurement uncertainties). However, from this analysis five pairs of locations, shown in Figure 8B, were identified to have dose rates that were the same within 1 – 2 % of the desired doses. These locations would allow for pairs of vials to be irradiated at the same dose rate.

The paired locations for which each pair was the same dose rate were 8/9, 4/5, 2/10, 1/6 and 3/7. The grid locations where the labeled vial samples were secured/positioned are shown in the photo as well as listed in the table below. Also in the table as are the associated dose rates and irradiation durations to achieve the 100 - 500 Mrad dose levels. Note the dose rates are associated with the estimated center of volume of the powder within the glass vials, which was ~4mm out from the surface of the wire grid.

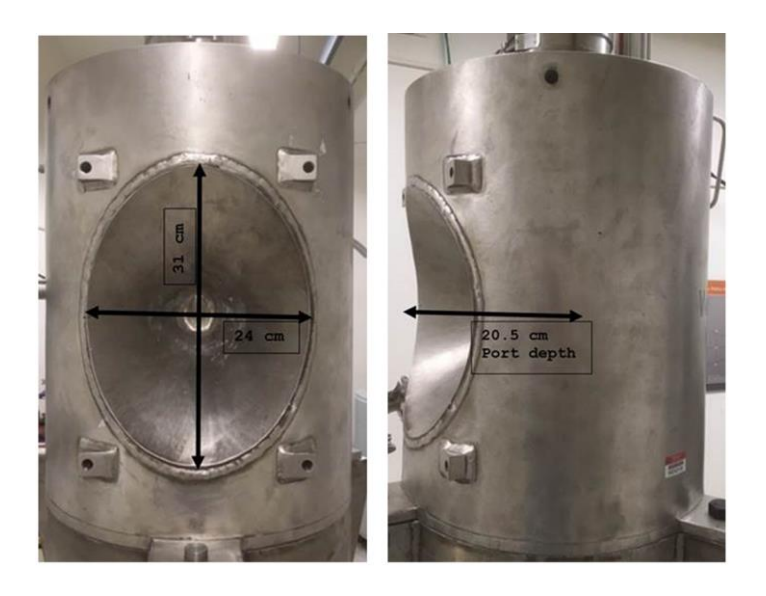


Figure 7: Radiation exposure chamber at PNNL.

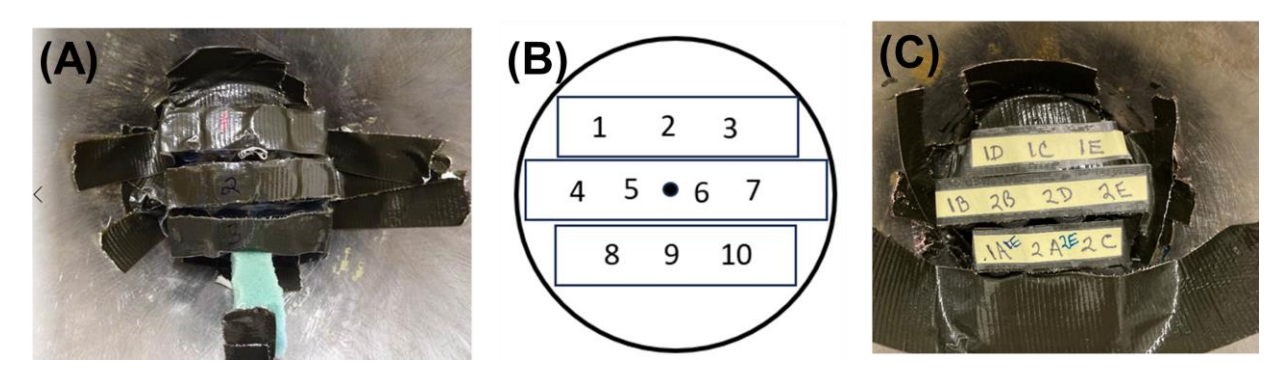


Figure 8: (A) Photograph of the wire mesh testing apparatus within the radiation chamber, (B) illustration of the ten dose locations, (C) the MOF samples loaded into the test chamber with corresponding IDs.

Table 2: Summary of Sample IDs and Corresponding Doses.

| MOF   | Sample ID | Dose<br>(Mrad) |
|-------|-----------|----------------|
|       | 1A        | 100            |
|       | 1B        | 200            |
| CuBTC | 1C        | 300            |
|       | 1D        | 400            |
|       | 1E        | 500            |
|       | 2A        | 100            |
|       | 2B        | 200            |
| CaSDB | 2C        | 300            |
|       | 2D        | 400            |
|       | 2E        | 500            |

Sample vials 1E and 2E were initially located at the lowest dose rate locations (3/7). After sample vials 1A and 2A (located at the highest dose rate locations of 8/9) obtained their 100 Mrad and removed, samples 1E and 2E were moved to locations 8/9 to take advantage of the higher dose rate and reduce the irradiation duration. Note that, when samples were removed after achieving the desired dose level, they were replaced with empty vials to help ensure other vials remained in their location and did not shift.

Table 3: Summary of samples at each identified location, the dose rate at location, time at each location, and total dose received for each pair of samples.

| Grid<br>Pair | Sample ID at Location | Dose Rate<br>(Mrad/h) | Irradiation<br>Time (h) | Total Dose<br>(Mrad) |
|--------------|-----------------------|-----------------------|-------------------------|----------------------|
| 1/6          | 1D/2D                 | 2.04                  | 196.2                   | 400                  |
| 2/10         | 1C/2C                 | 2.07                  | 145.1                   | 300                  |
| 3/7          | 1E/2E                 | 1.93                  | 42.5                    | 82                   |
| 4/5          | 1B/2B                 | 2.13                  | 94.0                    | 200                  |
| 8/9          | 1A/2A                 | 2.86                  | 42.5                    | 100                  |
| 8/9          | 1E/2E                 | 2.36                  | 177.4                   | 418                  |

#### 4.0 Impacts of γ-Radiation on Sorbents

Post radiation, all the samples were collected, and a noticeable discoloration had occurred to the vials, see

(A)

(B)

Figure 9.. It should be noted that handling of vials post-irradiation was done carefully due to potential breakage caused by embrittlement of the glass. Both MOF samples were fully characterized using FTIR, PXRD, gas adsorption analysis to elucidate the effects irradiation on the structure and properties of the materials.

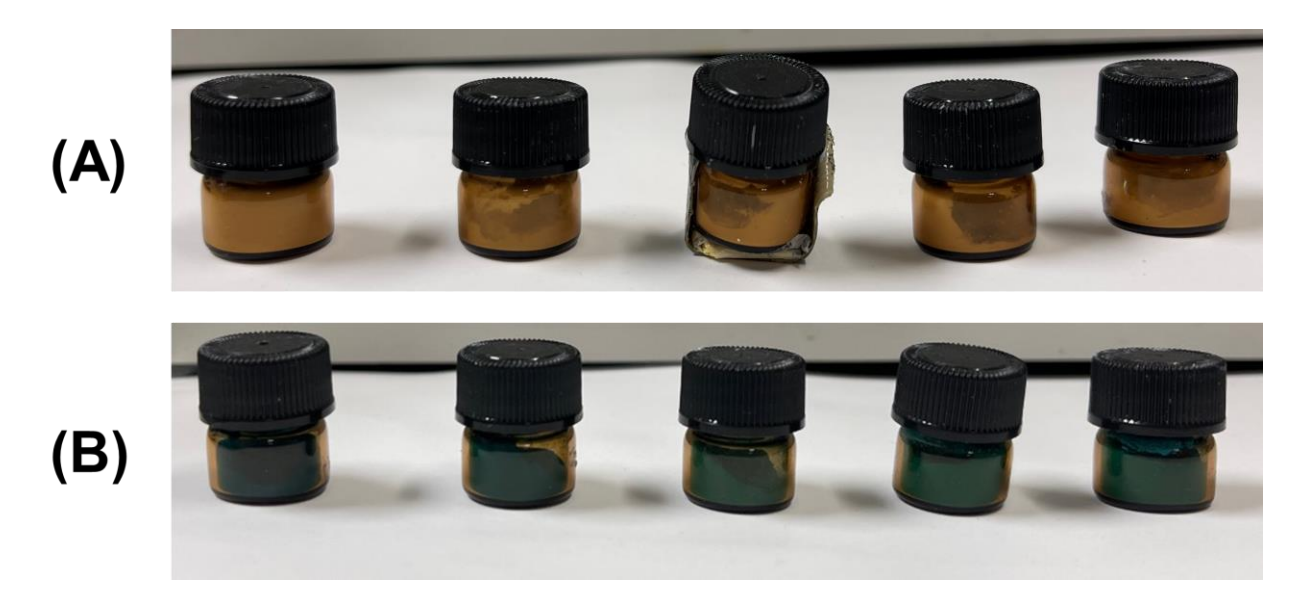


Figure 9: Images of radiation exposed vials (doses from left to right 100, 200, 300, 400, and 500 Mrad:) for (A) CaSDB and (B) CuBTC powders.

#### 4.1 CuBTC

First, optical images and visual inspections were done to each dose rate to determine if any discoloration had occurred due to gamma-exposure. Pristine CuBTC was teal in color, due to the presence of Cu<sup>2+</sup> as the metal nodes of the framework, see Figure 18A. As shown form Figure 18B, the only subtle changes occurred even after a 500 Mrad dose of gamma-radiation. As, shown in Figure 11, none of the doses showed any substantial color change for the CuBTC powders. Primarily, a lightening of the color was observed. In some samples, notably 300 Mrad exposed CuBTC, the color of the MOF yellowed. This was determined to be the result of the type and position of lighting used to image the powders and did not accurately represent any real change due to irradiation.

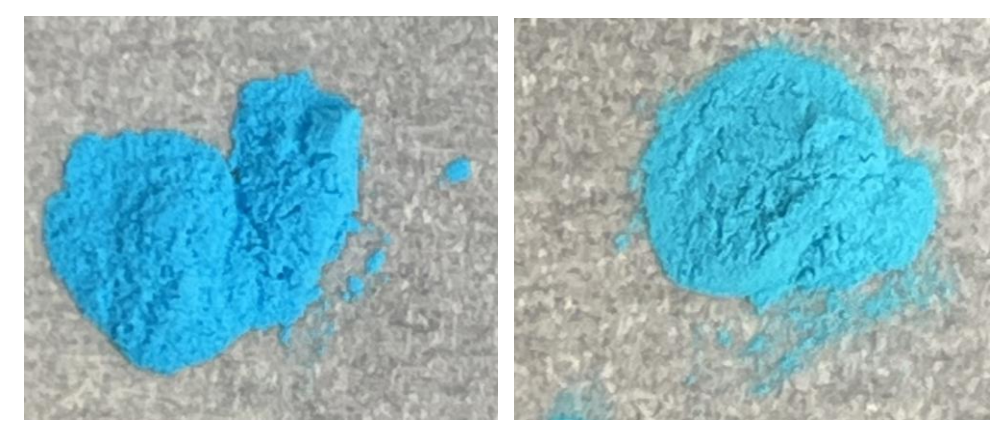


Figure 10: Images of pristine (Left) and 500 Mrad (right) radiation exposed CuBTC samples.

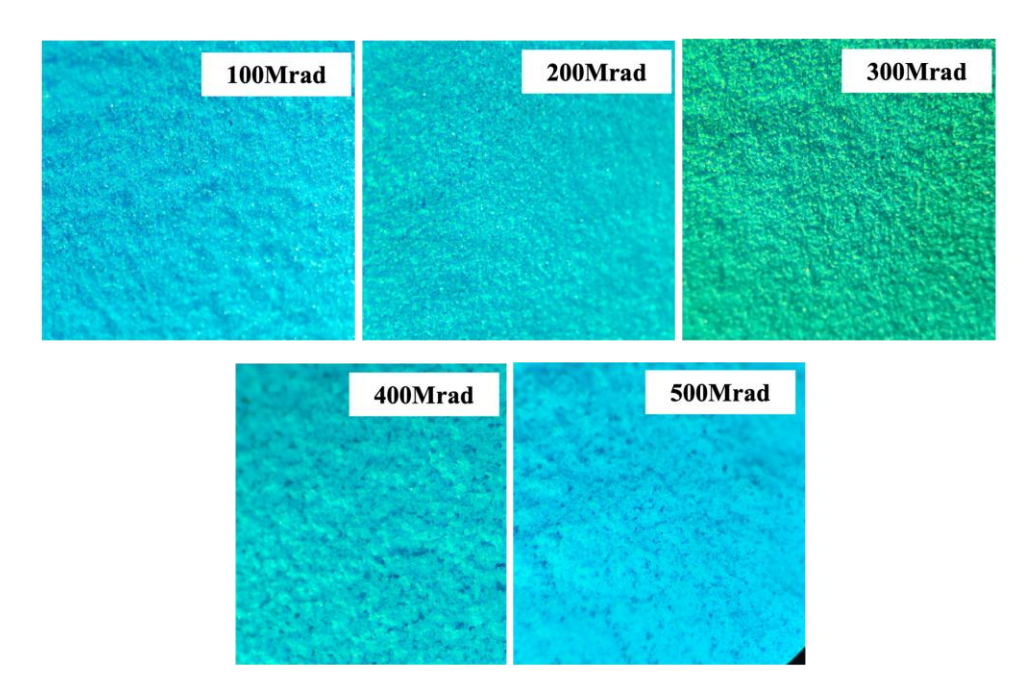


Figure 11: Light microscope images of CuBTC post-irradiation at 100, 200, 300, 400, and 500 Mrad.

As shown in Figure 12, no bulk morphological changes to the CuBTC crystallites occurred post-irradiation. This indicated that the radiation did not substantially degrade the CuBTC framework. Furthermore, the crystallite size of CuBTC remained identical pre- and post-irradiation. However, this characterization does not probe internal structural changes that may have taken place.

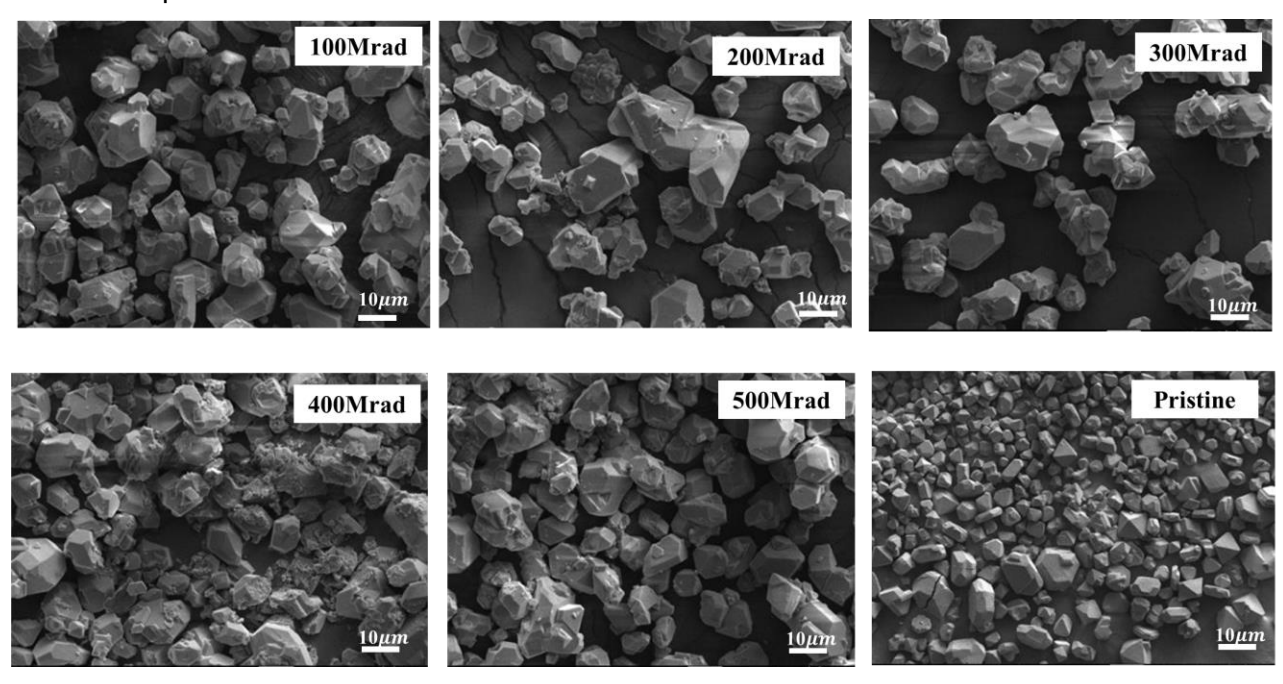


Figure 12: Comparison of SEM image of (A) pristine CuBTC to irradiated CuBTC powders at (B) 100, (C) 200, (D) 300, (E) 400, and (F) 500 Mrad.

Analysis of structural changes to the CuBTC framework post-irradiation was performed using PXRD. As shown in Figure 13A, no substantial changes to the framework were observed in the PXRD patterns of the irradiated samples. The no additional crystalline phases formed, and the overall crystallinity (i.e., long term order) of the samples did not change substantially. However, indicators of minor degradation were observed from the PXRD patterns. Slight decreases in total crystallinity and changes in the ratios of the reflections. This was particularly evident for the lowest angle reflections, typically representative of the pore structure of the MOF. For CuBTC, the intensity for the reflection at 6.8° 20, representing the (200) plane, was compared to the reflection at about 9.6° 20, which represents the (222) plane, illustrated in Figure 13C. The ratio of the reflections, summarized in Table 4, decreased after irradiation of the MOF. The decrease in (200) reflection intensity suggested possible occupancy of the pores by products formed due to radiation damage to the framework. However, the extend of change was not linear with respect to dose amount. Shown in Figure 13B, the relative ratio of the (200) and (220) reflections decrease gradually until the 300 Mrad dose, before it dropped dramatically. Then the reflection ratio began to increase at doses of 400 and 500 Mrad. Decreases in the low angle reflections, representative of the pore structure, indicated the possible formation of guests within the pore space due to structural degradation. Combine with the slow decrease in total pattern intensity (i.e., CuBTC crystallinity) indicated that only small-local domains of the framework were changing. Furthermore, the recovery of reflection ratio at higher doses may be due to further degradation of the initially formed products by the additional radiation. This led to reduction in quest occupancy in the pore space an increase in the (200) reflection intensity.

Table 4. Comparison of the intensity ratio of the (200) reflection ( $R_{(200)}$ ) and the (220) reflection ( $R_{(220)}$ ) obtained from CuBTC PXED patterns pre- and post-irradiation and the relative change in the ratios compared to the pristine (0 Mrad) powder.

| Dose<br>(Mrad) | R <sub>(200)</sub> /R <sub>(220)</sub> | Relative Reflection<br>Ratio (%) |
|----------------|--|----------------------------------|
| 0              | 1.55                                   | 100                              |
| 100            | 1.36                                   | 88.0                             |
| 200            | 1.26                                   | 81.5                             |
| 300            | 0.72                                   | 46.3                             |
| 400            | 0.97                                   | 62.8                             |
| 500            | 1.04                                   | 67.2                             |

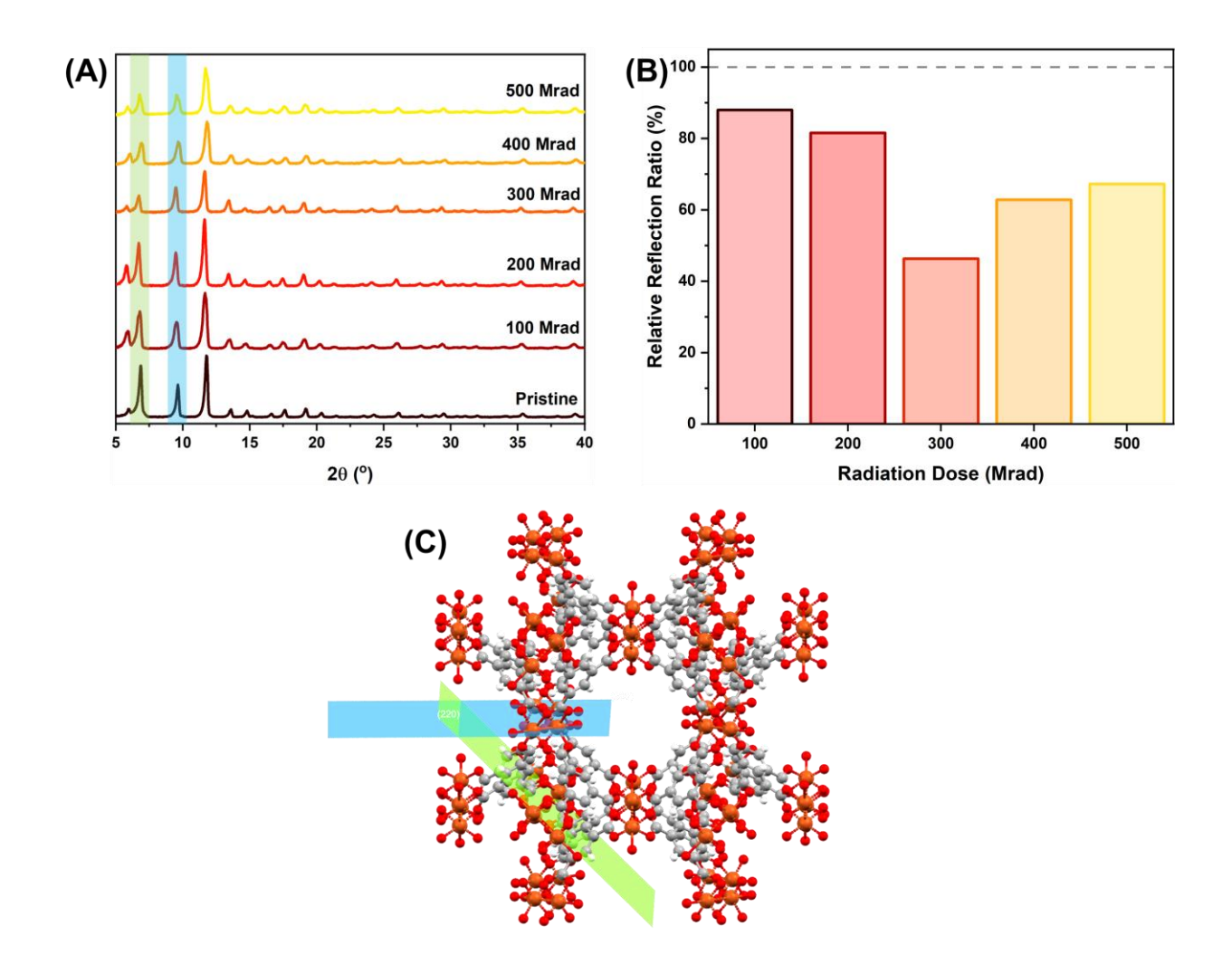


Figure 13: Comparison of (A) PXRD patterns of CuBTC powders pre- and post-radiation with (200) and (220) reflections highlighted green and blue, respectively, and (B) relative reflection ratio of  $R_{(200)}/R_{(220)}$  of irradiated samples compared to pristine CuBTC; (C) illustration of the (200) plane (blue) and (220) plane (green) of CuBTC.

The local structures of the irradiated CuBTC samples were probed using FTIR and NMR spectroscopies. NMR provided no tangible results due to the paramagnetic nature of the Cu<sup>2+</sup> metal centers in the framework. Collected FTIR spectra, shown in Figure 14A, matched similarly results to the PXRD, and showed minimal changes to the CuBTC structure. No new peaks were observed which indicated that the no substantial changes in framework bonding had occurred. However, shown in Figure 14B, there were subtle changes to the spectra near 1700 cm<sup>-1</sup>. The minor peak in the FTIR spectra of CuBTC at this position represents a carboxylic acid vibrational mode of free (i.e., extra-framework) BTC linker left over within the pores from synthesis. This was determined to be free BTC linker due to the higher chemical shift compared to the coordinated framework linkers.<sup>12, 13</sup> PXRD was not able to identify the presence of the linker due to the non-periodic nature of the free linker within the pores of the MOF. Furthermore, the change in intensity of the peak suggested that the amount of free linker changed with dose amount. The peak intensity increased to a maximum intensity at 300 Mrad, then decreased to near the initial intensity by 500 Mrad. This suggested that the radiation caused framework linkers to break coordination from the framework due to radiation-induced structural changes, while at higher doses the

radiation caused degradation of the free linkers within the pores. Which aligns well with trends observed in PXRD analysis.

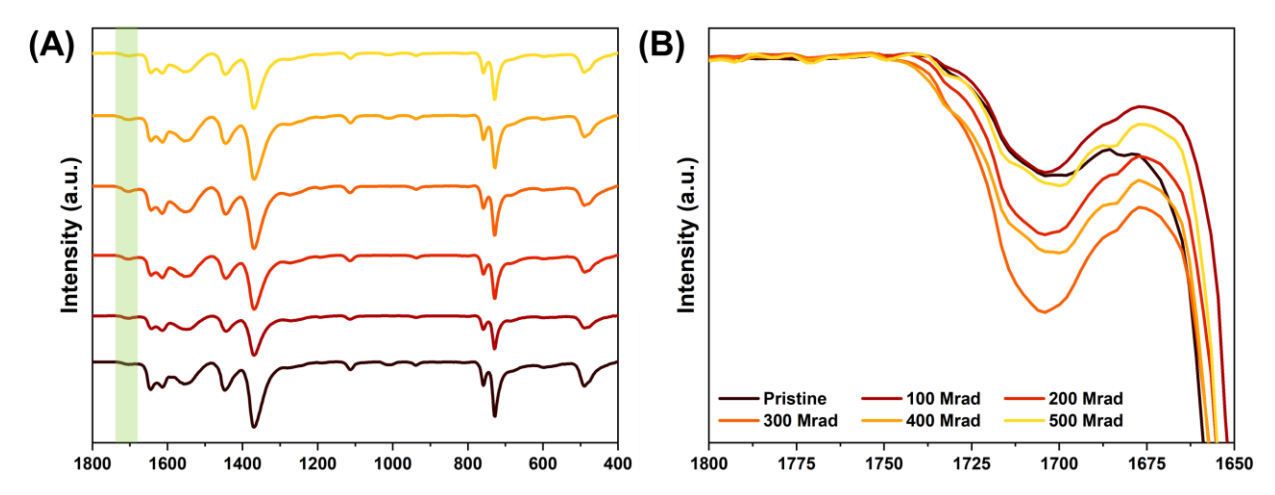


Figure 14: FTIR spectra of pre- and post-irradiation CuBTC samples between (A) 400 and 1800 cm<sup>-1</sup> with the green highlighted region representing the free BTC carboxylic acid shift and (B) a zoomed spectra depicting the changes to the free BTC carboxylic acid shift.

Examination of the textural properties was performed to examine the effects of radiation on the internal surface area, porosity, and gas uptake capacities. As shown in Figure 15A, the N<sub>2</sub> gas uptake (at 77 K) of CuBTC decreased post-radiation exposure. Like PXRD, the changes did not decrease proportionally with radiation dose. The N<sub>2</sub> adsorption decrease dramatically by the 300 Mrad dose then increased for the subsequent doses. Examination of the calculated BET values, summarized in Table 5, showed the same trend as the  $R_{(200)}/R_{(220)}$  ratio. Again, the 300 Mrad exposed samples showed the largest decrease which recovered slightly with increasing doses. Notably, the isotherm shape did not change substantially post-dose indicating the material maintained microporosity at all doses. Furthermore, this indicated that the pore structure was not significantly changed and remained whole over the bulk of the material. However, examination of the pore size distribution, shown in Figure 16, showed that the total porosity and distribution of the porosity of CuBTC decreased post-dose. Additionally, at 300 Mrad dose the CuBTC pore size distribution was the widest and the incremental pore volume was the lowest. While, the pore size distribution began to regain the character of the pristine framework, matching well with the uptake and surface area, along with additional distinct pore sizes between 0.75 nm and 1 nm after a 500 Mrad dose. Altogether, these results support the hypothesis that the initial radiation exposure degraded the MOF through changes to the local coordination structure that occupied the pores and reduced gas uptake. These results further suggest that the radiation-induced degradation products were further degraded leading to increase gas accessibility of the pore space, while addition defects were generated increasing the porosity of the material.

Table 5. BET surface areas of CuBTC samples pre- and post-irradiation and the relative change in surface areas compared to the pristine (0 Mrad) powder.

| Dose<br>(Mrad) | BET Surface Area<br>(m²/g) | Relative BET<br>(%) |
|----------------|----------------------------|---------------------|
| 0              | 1364 ± 60                  | 100                 |
| 100            | $1345 \pm 57$              | 99 ± 4              |
| 200            | 1047 ± 35                  | 77 ± 3              |

| 300 | 650 ± 12     | 48 ± 1 |
|-----|--------------|--------|
| 400 | $760 \pm 13$ | 56 ± 1 |
| 500 | 869 ± 13     | 64 ± 1 |

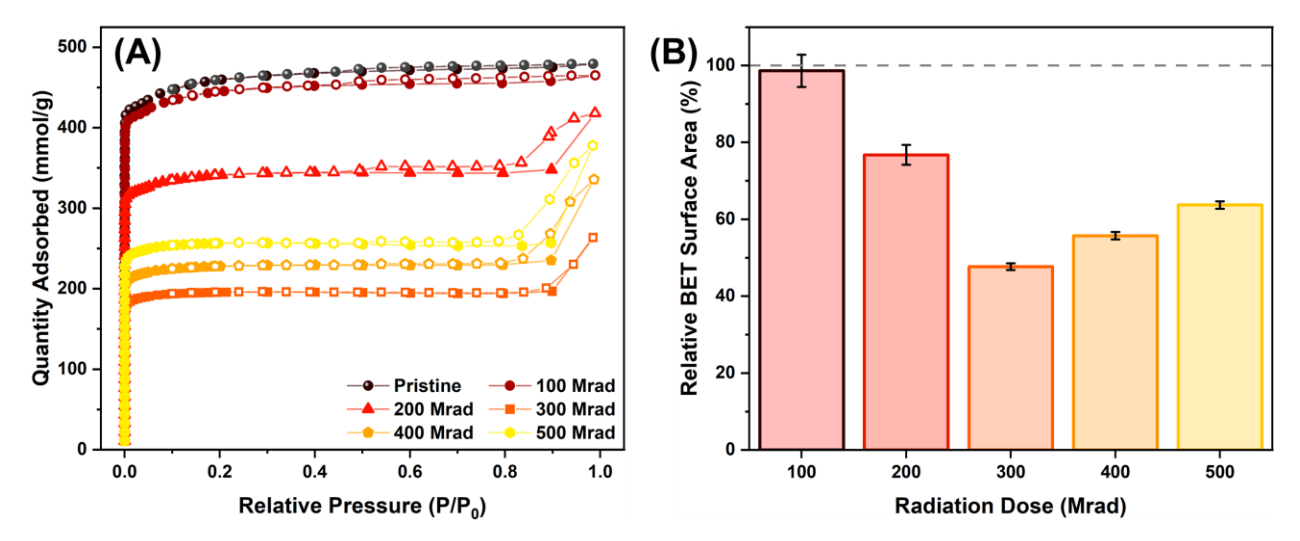


Figure 15: Comparison of (A) N<sub>2</sub> gas adsorption isotherms at 77K of pre- and post-irradiation CuBTC samples and (B) the relative BET of CuBTC post-radiation.

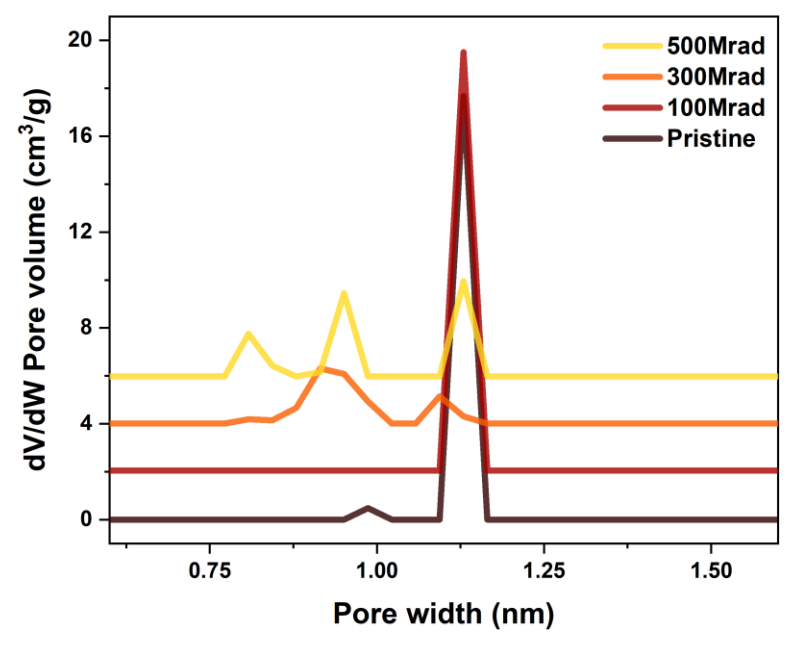


Figure 16: Comparison of pore volume distribution of CuBTC pre- and post-irradiation. All data is offset by 2 cm<sup>3</sup>/g.

The changes to the porosity of CuBTC induced by radiation were also examined to determined how this effected noble gas adsorption. As shown in Figure 17, gas adsorption isotherms for Xe and Kr were collected at  $-78^{\circ}$ C (195 K) on the post-irradiated CuBTC powders. Interestingly, the Xe adsorptions did not show the same adsorption trends as N<sub>2</sub>. Xe uptake decrease proportionally to the dose received, see Figure 17A, from a maximum uptake of 6.3 mmol/g to 3.9 mmol/g for

100 and 500 Mrad doses, respectively. This was likely the result of the about 120 K difference in temperature. At 77 K, restriction of the pore to near the kinetic diameter of  $N_2$  results in decrease gas uptake, which is not observed at higher temperatures. Kr showed some variation in the adsorption trend compared to Xe. The Kr uptake increased with dose up to 200 Mrad, then decreased with the 500 Mrad dose having the lowest gas uptake. Notably, comparing the ratio of the Xe/Kr gas uptake at 1 bar, shown in Table 6, indicated that the selectivity of CuBTC decreased with increasing radiation dose. This resulted in the same total capacities at 1 bar for both gases. However, based on the low-pressure adsorptions Xe will likely be slighted favored over Kr under practical concentrations even after a 500 Mrad dose. Though the Xe loading in CuBTC is decreased, Xe adsorption in CuBTC is extremely steep at low pressures and very selective to Xe over Kr. The CuBTC could be an ideal candidate for further investigation.

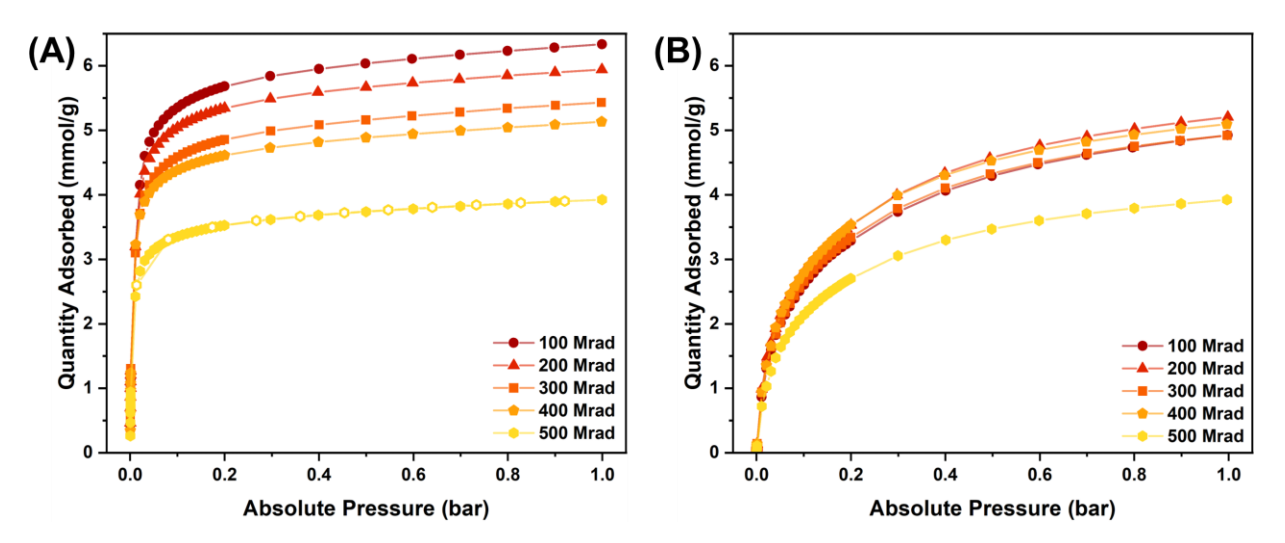


Figure 17: Gas adsorption isotherms of irradiated CuBTC powders at  $-78^{\circ}$ C for the noble gases (A) Xe and (B) Kr.

Table 6. Xe and Kr uptakes at 1 bar and associated Xr/Kr ratio for CuBTC samples pre- and post-irradiation.

| Dose<br>(Mrad) | Xe Uptake<br>(mmol/g) | Kr Uptake<br>(mmol/g) | Xe/Kr |
|----------------|-----------------------|-----------------------|-------|
| 100            | 6.3                   | 4.9                   | 1.29  |
| 200            | 6.0                   | 5.2                   | 1.15  |
| 300            | 5.4                   | 5.1                   | 1.06  |
| 400            | 5.1                   | 4.9                   | 1.04  |
| 500            | 3.9                   | 3.9                   | 1.00  |

#### 4.2 CaSBD



Figure 18: Photographs of pristine CaSDB (left) and CaSDB post 500 Mrad irradiation dose. (right).

Unlike CuBTC, CaSDB showed apparent visual differences post radiation. Shown in Figure 18, the CaSDB MOF yellowed after exposure to gamma radiation. Optical images of the irradiated CaSDB samples (see Figure 19) did not show a noticeable trend in the degree of color change. Color changes in Ca-MOFs are highly impacted by the organic features within the structure. The color change observed suggested that the organic portion of the MOF underwent a chemical change induced by the radiation.

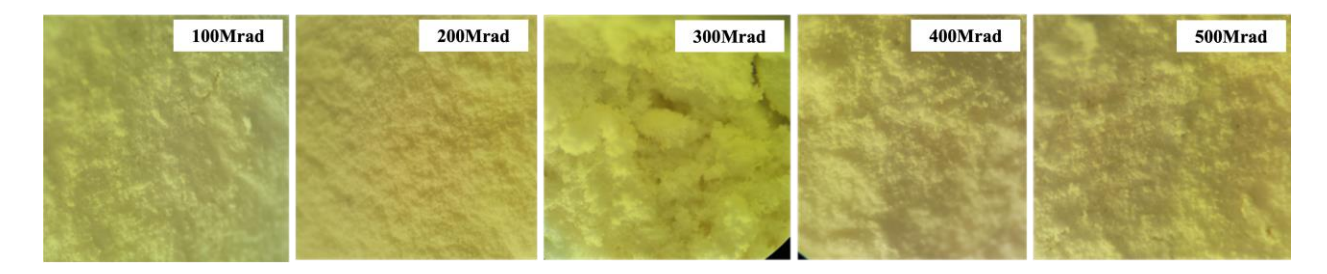


Figure 19: Optical images radiation exposed CaSDB samples.

To elucidate the origin of the color change and the impact of the radiation dose on the structure of CaSDB the same characterization illustrated for CuBTC was performed. From SEM images, shown in Figure 20, the bulk morphology of CaSDB did not substantially change. The noticeable pitted surface and irregular particle size and shapes observed in the irradiated samples was also observed in the pristine CaSDB powder. Like CuBTC this indicated that limited structural transformation of the framework occurred. However, further structural characterization was required to elucidate these changes.

As shown in Figure 21, no substantial changes in the FTIR spectra were observed. This further reinforced that limited structural degradation had occurred. However, like CuBTC, the FTIR spectra did show guest molecules within the framework. The peak near 1680 cm<sup>-1</sup> represented free SDB linker within the samples. Though the CaSDB materials were thoroughly washed and PXRD verified removal of unreacted linker, residual non-crystalline linker remained in the pores. Furthermore, this chemical shift may represent defects sites within the framework due to one carboxylic acid group of a linker not being coordinated due to a missing metal. Regardless of origin, the intensity of the chemical shift increased at 200 Mrad dose before decreasing and

becoming negligible at a dose of 500 Mrad. This trend aligned with those observed with CuBTC and suggested a similar radiation-induced degradation mechanism occurred for CaSDB. Which is that linker guest molecules from local degradation sites occupy and block the MOF pores before further degradation of the guest by the increased radiation.

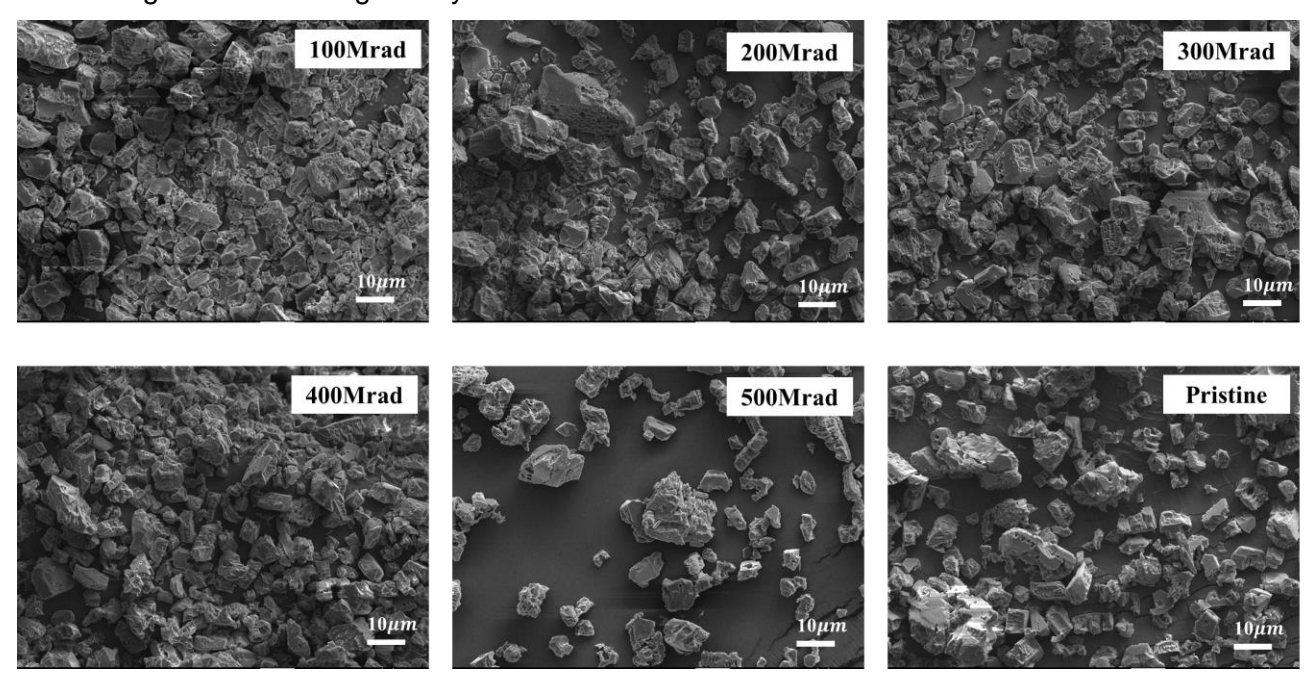


Figure 20: SEM images of CaSDB powders pre- and post-irradiation.

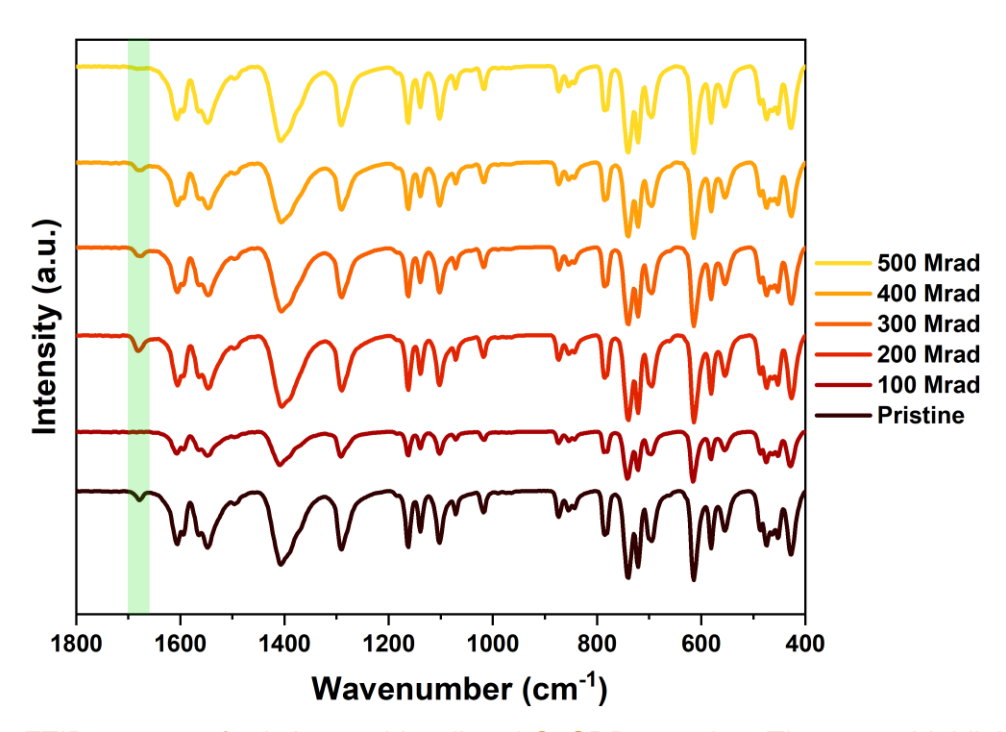


Figure 21: FTIR spectra of pristine and irradiated CaSDB samples. The green highlighted peak at 1680 cm<sup>-1</sup> represents the free linker carboxylic acid chemical shift.

PXRD patterns of the pristine as well as irradiated CaSDB samples presented in Figure 22, shoed less structural changes post-radiation compared to CuBTC. Overall, there was slight changes in the in the total pattern intensities, however, the relative peaks intensities remained nearly constant throughout. This suggested that the long-range structure was not substantially affected by the gamma-radiation. Notably, the 200 Mrad exposed CaSDB showed much lower intensities compared to the other doses. However, the intensity of the reflection at  $8^{\circ}$  20 did change slightly, indicating a possible change in the guest occupancy within the pores. Comparison of the  $6.8^{\circ}$  20 reflection intensity showed that relative to the pristine CaSDB the 200 Mrad dose sample showed the lowest intensity while the 500 Mrad dose samples showed the largest intensity. This again aligned with the proposed mechanism of structural change upon radiation exposure.

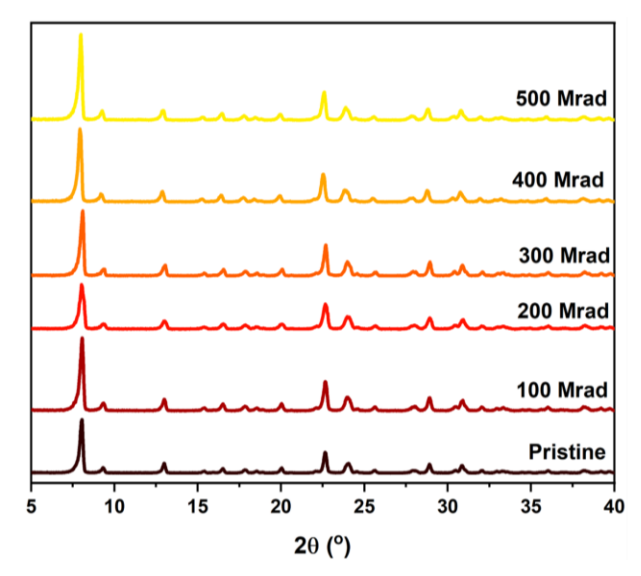


Figure 22: Comparison of PXRD patterns of CaSDB powders pre- and post-radiation.

Table 7: Rietveld refinement of the unit cell parameters for pristine and irradiated CaSDB samples

| Dose   | Unite Cell Parameter (Å) |       |        |  |
|--------|--------------------------|-------|--------|--|
| (Mrad) | а                        | b     | С      |  |
| 0      | 11.832                   | 5.585 | 22.846 |  |
| 100    | 11.841                   | 5.591 | 22.857 |  |
| 200    | 11.852                   | 5.590 | 22.844 |  |
| 300    | 11.861                   | 5.589 | 22.827 |  |
| 400    | 11.864                   | 5.592 | 22.846 |  |
| 500    | 11.863                   | 5.592 | 22.853 |  |

Further analysis of the PXRD results was performed to gain additional insights into the structural changes that occurred because of gamma-radiation. Rietveld refinement was performed on the unit cell parameters of the irradiated and pristine CaSDB samples. The results are presented in Table 7 and showed that though small (< 0.5%) there were changes in the unit cell post-radiation. As shown in Figure 23, the amount of change and the direction (i.e., increasing or decreasing) of change for each parameter differed. Overall, a general expansion of the unit cell

was observed which is consistent with the trend in MOF structural change. For the unit cell parameter, *a*, an increase occurred as the radiation dose increased until 400 Mrad, beyond which remained nearly the same. The unit cell parameter *b* showed a relatively constant increase at all doses, While, the cell parameter *c* showed the smallest changes, increasing at the extremes while decreasing at 300 Mrad.

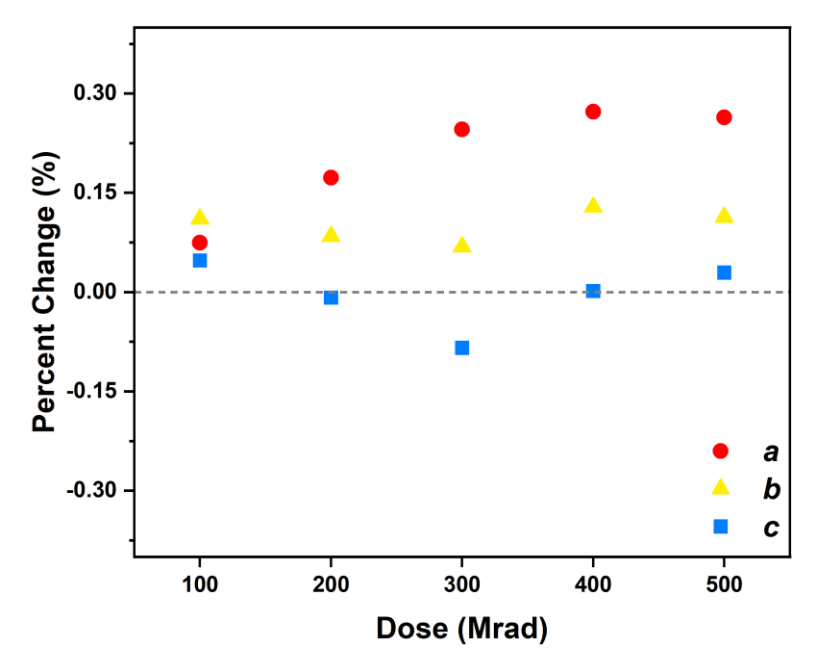


Figure 23: Percentage change in unit cell parameters a (red circles), b (yellow triangles), and c (blue squares) from Rietveld refinement of CaSDB post-irradiation. The grey dashed line represents the pristine cell parameters.

Gas adsorption analysis was performed to determine how these subtle structural changes impacted the porosity and gas uptake. Prior to obtaining surface area measurements, samples were degassed at 150°C overnight to remove any volatile impurities, such as moisture or residual solvents present. As shown in Figure 24, the N<sub>2</sub> gas adsorption isotherms were dramatically impacted by the gamma irradiation. Post exposure all doses showed loss of the typical type I isotherm indicative of a microporous material and in fact showed no N<sub>2</sub> adsorption. This suggested that the materials had become non-porous. However, this did not align with the much smaller structural changes observed through FTIR, SEM and PXRD analysis, discussed above. This suggested that the observed change in the N<sub>2</sub> adsorption was due to the kinetic limitations of N<sub>2</sub> adsorption at 77 K. If a material's pores are near the kinetic diameter of N2 then the adsorption of the gas at cryogen temperature is slowed beyond typical experiments' equilibration times and no gas adsorption is observed. This suggested that the local-structural changes observed in FTIR and PXRD impact the porosity of CaSDB significantly more than CuBTC. This is likely the results of the smaller pores and pore shape of CaSDB compared to CuBTC. Additionally, thorough washing of the samples did not change the adsorption results, demonstrating that pore structure had changed, and the pores were not blocked by free SDB linkers.

These kinetic limitation in the gas adsorption can be overcome by increasing the analysis temperature, however, N<sub>2</sub> adsorption decreases substantially at higher temperatures. Therefore, other gases are used instead to test the porosity of these materials.

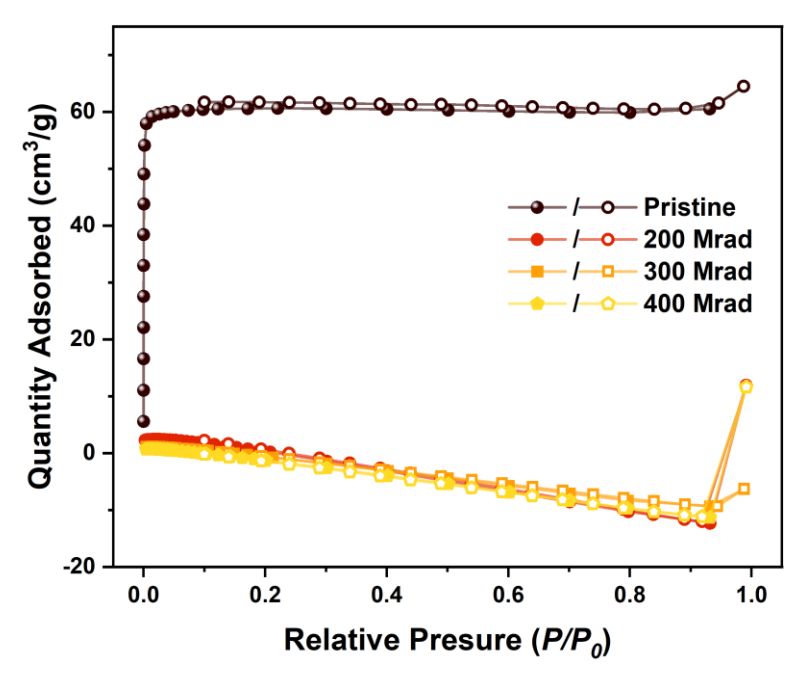


Figure 24: N<sub>2</sub> gas adsorption isotherms of pristine CaSDB and selected CaSDB post-irradiation at 200, 300, and 400 Mrad.

#### 5.0 Conclusion

The exemplar noble gas sorbents CuBTC and CaSDB were obtained and fully characterized before exposure to high doses of gamma-radiation for the first time. Post exposure the samples were recharacterized to elucidate the impacts of radiation on the structure and gas adsorption properties of the MOFs. From PXRD and FTIR analysis of the two MOFs post-irradiation no substantial structural changes were observed. Though the analysis indicated that small changes in the local structure occurred. Gas adsorption analysis using N2, Xe, and Kr showed that these subtle changes had a large impact on the porosity and gas uptake properties of both materials. In the case of CuBTC, the pore size and distribution of pores in the framework were decreased which led to reduced surface area with increasing radiation dose. The smaller pore size of CaSDB was more sensitive to the radiation compared to CuBTC in terms of surface area. This was surprising as PXRD. SEM analysis suggested that the framework was more stable to the radiation compared to CuBTC. These results indicated that the small local changes led to pore blockage and occupancy and that more dose can reverse some of the lost surface area. Additionally, this work demonstrated methodology that can help identify and predict the impact on material properties (the reflection intensity ratios versus surface area trends for example). Altogether, this work demonstrates that though the frameworks of CuBTC and CaSDB were stable to radiation the porosity was very sensitive to the small changes that the radiation causes.

#### 6.0 Future Work

Moving forward this project seeks to better understand the fundamental changes occurring to the pores and expand the analysis to more practical material. To achieve this additional characterization methods are being utilized in current and subsequent experiments. Powder samples of irradiated CuBTC and CaSDB are being analyzed using a synchrotron X-ray source to obtain data relevant to the local structure of the frameworks. Furthermore, solid state NMR

experiments are being optimized probe the local structure as well. Gas characterization will include carbon dioxide gas adsorption analysis at  $0^{\circ}$ C to avoid complications due to kinetic effects with  $N_2$  adsorption analysis. Additional engineered forms of the MOFs will be examined. Previous work has identified granulized pressed MOF and MOF-polymer composite beads as promising engineered forms of CuBTC and CaSDB. Studies are planned to irradiate these forms and form manipulation influence the radiation stability of the MOFs. Characterization insight from this work will guide experiments for the engineered MOF studies.

#### 7.0 References

- (1) Filak-Mędoń, K.; Fornalski, K. W.; Bonczyk, M.; Jakubowska, A.; Kempny, K.; Wołoszczuk, K.; Filipczak, K.; Żerańska, K.; Zdrojek, M. Graphene-based nanocomposites as gamma- and X-ray radiation shield. *Sci. Rep.* **2024**, *14* (1), 18998. DOI: 10.1038/s41598-024-69628-5
- (2) Nambiar, S.; Yeow, J. T. W. Polymer-Composite Materials for Radiation Protection. *ACS Appl. Mater. & Interfaces* **2012**, *4* (11), 5717-5726. DOI: 10.1021/am300783d
- (3) Christian, J. H.; Teprovich, J. A.; Wilson, J.; Nicholson, J. C.; Truong, T. T.; Kesterson, M. R.; Velten, J. A.; Wiedenhöver, I.; Baby, L. T.; Anastasiou, M.; et al. Developing radiation tolerant polymer nanocomposites using C60 as an additive. *RSC Adv.* **2016**, *6* (47), 40785-40792. DOI: 10.1039/C6RA01126H
- (4) Hanna, S. L.; Rademacher, D. X.; Hanson, D. J.; Islamoglu, T.; Olszewski, A. K.; Nenoff, T. M.; Farha, O. K. Structural Features of Zirconium-Based Metal–Organic Frameworks Affecting Radiolytic Stability. *Ind. Eng. Chem. Res.* 2020, 59 (16), 7520-7526. DOI: 10.1021/acs.iecr.9b06820
- (5) Banerjee, D.; Simon, C. M.; Plonka, A. M.; Motkuri, R. K.; Liu, J.; Chen, X.; Smit, B.; Parise, J. B.; Haranczyk, M.; Thallapally, P. K. Metal-organic framework with optimally selective xenon adsorption and separation. *Nat. Commun.* **2016**, *7* (1), ncomms11831. DOI: 10.1038/ncomms11831
- (6) Ahmed, A.; Hodgson, N.; Barrow, M.; Clowes, R.; Robertson, C. M.; Steiner, A.; McKeown, P.; Bradshaw, D.; Myers, P.; Zhang, H. Macroporous metal—organic framework microparticles with improved liquid phase separation. *J. Mater. Chem. A* 2014, 2 (24), 9085-9090. DOI: 10.1039/C4TA00138A
- (7) Pang, S. H.; Han, C.; Sholl, D. S.; Jones, C. W.; Lively, R. P. Facet-Specific Stability of ZIF-8 in the Presence of Acid Gases Dissolved in Aqueous Solutions. *Chem. Mater.* 2016, 28 (19), 6960-6967. DOI: 10.1021/acs.chemmater.6b02643
- (8) Riley, B. J.; Chong, S.; Kuang, W.; Varga, T.; Helal, A. S.; Galanek, M.; Li, J.; Nelson, Z. J.; Thallapally, P. K. Metal–Organic Framework–Polyacrylonitrile Composite Beads for Xenon Capture. *ACS Appl. Mater. & Interfaces* **2020**, *12* (40), 45342-45350. DOI: 10.1021/acsami.0c13717
- (9) Hastings, A. M.; Fairley, M.; Wasson, M. C.; Campisi, D.; Sarkar, A.; Emory, Z. C.; Brunson, K.; Fast, D. B.; Islamoglu, T.; Nyman, M.; et al. Role of Metal Selection in the Radiation Stability of Isostructural M-UiO-66 Metal—Organic Frameworks. *Chem. Mater.* **2022**, *34* (18), 8403-8417. DOI: 10.1021/acs.chemmater.2c02170
- (10) Gilson, S. E.; Fairley, M.; Julien, P.; Oliver, A. G.; Hanna, S. L.; Arntz, G.; Farha, O. K.; LaVerne, J. A.; Burns, P. C. Unprecedented Radiation Resistant Thorium–Binaphthol Metal–Organic Framework. *J. Am. Chem. Soc.* **2020**, *142* (31), 13299-13304. DOI: 10.1021/jacs.0c05272
- (11) Ma, C.; Liu, H.; Wolterbeek, H. T.; Denkova, A. G.; Serra Crespo, P. Effects of High Gamma Doses on the Structural Stability of Metal–Organic Frameworks. *Langmuir* **2022**, *38* (29), 8928-8933. DOI: 10.1021/acs.langmuir.2c01074
- (12) Volkringer, C.; Leclerc, H.; Lavalley, J.-C.; Loiseau, T.; Férey, G.; Daturi, M.; Vimont, A. Infrared Spectroscopy Investigation of the Acid Sites in the Metal–Organic Framework Aluminum Trimesate MIL-100(AI). *J. Phys. Chem. C* **2012**, *116* (9), 5710-5719. DOI: 10.1021/jp210671t
- (13) Socrates, G. Infrared and Raman Characteristic Group Frequencies; Wiley, 2001.

## 8.0 Acknowledgements

We thank DOE – Office of Nuclear Energy - Molten Salt Research program for financial support. We also would like to thank Dr. Patricia Paviet for support and encourangement,

# Pacific Northwest National Laboratory

902 Battelle Boulevard P.O. Box 999 Richland, WA 99354

1-888-375-PNNL (7665)

www.pnnl.gov